

WWU MÜNSTER
FACULTY OF MATHEMATICS AND COMPUTER SCIENCE

MASTER'S THESIS

MASTER OF SCIENCE MATHEMATICS

**Comparison of Boundary Element Fast Multipole
and Finite Element Methods for the solution
of the EEG forward problem**

Author

Paul Lunkenheimer
Mt. 426667

Supervisor

Prof. Dr. Carsten Wolters
Prof. Dr. Christian Engwer

December 14, 2021

Contents

1	Introduction	9
2	The Physiological Basis Underlying EEG Measurements	11
3	The Finite Element Methods of DUNEuro	15
3.1	A Partial Differential Equation for the Electric Potential	15
3.2	A Weak Formulation	17
3.3	The Finite Element Method	18
3.4	Source Models	22
3.4.1	The Partial Integration Model	22
3.4.2	The Saint Venant Model	23
3.5	The Transfer Matrix Approach	24
3.6	DUNEuro	26
4	The Boundary Element Fast Multipole Method	27
4.1	Integral Equations for the Electric Surface Charge Distribution	28
4.1.1	Modeling the Source Directly	28
4.1.2	Helmholtz Reciprocity – Modeling Electrode Stimulation	31
4.2	A Galerkin Approach	33
4.2.1	Modeling the Source Directly	33
4.2.2	Helmholtz Reciprocity	34
4.3	Computational Details	35
4.3.1	Use of the Fast Multipole Method	35
4.3.2	Interaction between Near Neighbors	37
4.3.3	Conservation Laws, Preconditioners and Mesh Refinement	39
5	The Fast Multipole Method	41
5.1	The Concept	42
5.2	Mathematical Details	47
6	Comparison Studies of DUNEuro and BEM-FMM	55
6.1	A Multi-layer Sphere Model	57
6.2	A Realistic Head Model	66
6.3	Conclusion and Outlook	71

List of Figures

2.1	Human head tissues[3] and cerebral cortex[1]	11
2.2	Neuron[4]	12
3.1	Realistic tetrahedral mesh[23]	20
4.1	Induced electric surface charge[56]	29
4.2	Kirchhoff's current law[56]	29
5.1	Far field interaction	42
5.2	Refinement levels of FMM	43
5.3	Near neighbor, well separated and interaction list	44
6.1	4-layer sphere model	57
6.2	4-layer sphere model mesh resolutions	58
6.3	4-layer sphere model with electrodes	59
6.4	4-layer sphere model RDM over mesh resolution	61
6.5	4-layer sphere model MAG over mesh resolution	61
6.6	4-layer sphere model RDM over source eccentricity	62
6.7	4-layer sphere model MAG over source eccentricity	63
6.8	4-layer sphere model time over mesh resolution	65
6.9	Realistic head model slice	66
6.10	Realistic head model compartments	67
6.11	Dipole in realistic head model	68
6.12	Realistic head model potential	70

List of Tables

- 6.1 4-layer head model 57
- 6.2 4-layer sphere meshes 58
- 6.3 Dipole sources 59
- 6.4 Realistic head model 66
- 6.5 Realistic head meshes 66
- 6.6 Realistic comparison difference measures 68
- 6.7 Realistic comparison runtime 69

Chapter 1

Introduction

The human brain as our “main control center” is the focus of research all over the world. Clinical applications such as brain surgery as well as brain research use and analyze measured neurological activity. Electroencephalography (EEG) is a non-invasive method to record the electric potential evoked by such activity at the head surface at a high time resolution.

For example, drug-resistant, focal epilepsy may be treated by surgically removing the source area of the epileptic seizures. It is essential to only operate on the affected section and to not damage any other, possibly vital parts of the brain. Thus, the epileptogenic zone has to be determined as accurate as possible in pre-surgical diagnosis. Measuring epileptic spikes via EEG and analyzing the data can aid in the localization. Even though the epileptogenic zone does not produce a signal measurable by EEG, it stimulates neighboring pyramidal cells which in turn produce a measurable signal. We formulate the inverse problem of EEG: Determining location, orientation and magnitude of the sources of neural activity in the brain based on measured voltages at the EEG electrodes. The inverse problem is also of interest for basic brain research.

A pre-requisite for solving the inverse problem is a solver for the forward problem of EEG. It aims at predicting the electric potential at the surface evoked by given sources inside the head. Doing so for thousands or even tens of thousands of sources allows approaches for the inverse problem to use the results together with real measured data and to determine the most likely explanation for the measured potential using state-of-the-art mathematical methods. Thus, the forward problem needs to be solved not only accurately but also efficiently due to the necessary high number of sources. Solvers can also be useful when stimulating the brain using electrodes at the head surface.

This work compares the performance of two solvers. The approaches implemented in the software DUNEuro are volume-based and solve for the electric potential via Finite Element Methods. The Boundary Element Fast Multipole Method (BEM-FMM) on the other hand models the electric charge distribution on tissue surfaces and the potential can then be derived using Coulomb’s law. At the core of the latter solver is the Fast Multipole Method (FMM), which approximates Coulombic particle interaction efficiently.

In the first chapter, a brief physiological basis is established and the mechanism underlying the measured EEG data is described. This knowledge is important to understand and justify the derivation of the physical models that the two solvers at hand are based upon.

The second chapter then uses this basis to arrive at a partial differential equation for the electric potential using Maxwell's equations. This is the foundation for the first solver implemented in DUNEuro. It is restated as a weak formulation for which existence and uniqueness of a solution can be shown. The Finite Element Method provides an approach to derive a linear equation which can then actually be implemented and solved numerically. Two different models for the neurological sources are presented leading to different linear problems and solutions for the Forward Problem. Furthermore, the transfer matrix approach is a major reason for the efficiency of this approach. Finally, an overview about implementation details of the realization in DUNEuro is given.

The next chapter introduces the boundary element fast multipole method (BEM-FMM). Two approaches are derived which are based on the same physical and mathematical idea of integral equations for the electric surface charge density formulated on tissue boundary surfaces. The first approach models the source directly while the second approach makes use of electrode stimulation which is connected to the forward problem via Helmholtz reciprocity. A Galerkin approach leads to a formulation as a linear system of equations. The resulting matrix-vector product can be computed up to a specified precision with the fast multipole method which sits at the core of BEM-FMM and is computationally feasible and efficient. Interaction between close charges are calculated in a more precise way and comments on conservation laws, preconditioners and mesh refinement are made.

The last chapter presents two comparison studies of the BEM-FMM and the two approaches implemented in DUNEuro. The first one makes use of a multi-layer sphere model for which an analytical solution exists. Meshes at different resolutions as well as sources at positions of increasing complexity are investigated and different error measures are compared. Additionally, we look at the runtime of the methods. The second study was conducted on a realistic head model. Finally, a conclusion of the two studies is given and we present an outlook.

Chapter 2

The Physiological Basis Underlying EEG Measurements

This chapter aims at summarizing relevant physiology of the brain in order to allow an understanding of the solvers for the Forward Problem of EEG presented in the chapters thereafter. Most of the following can be found in any standard neuroscience textbook and follows [1]. Additionally, a review of relevant facts for the EEG forward problem is given in [2].

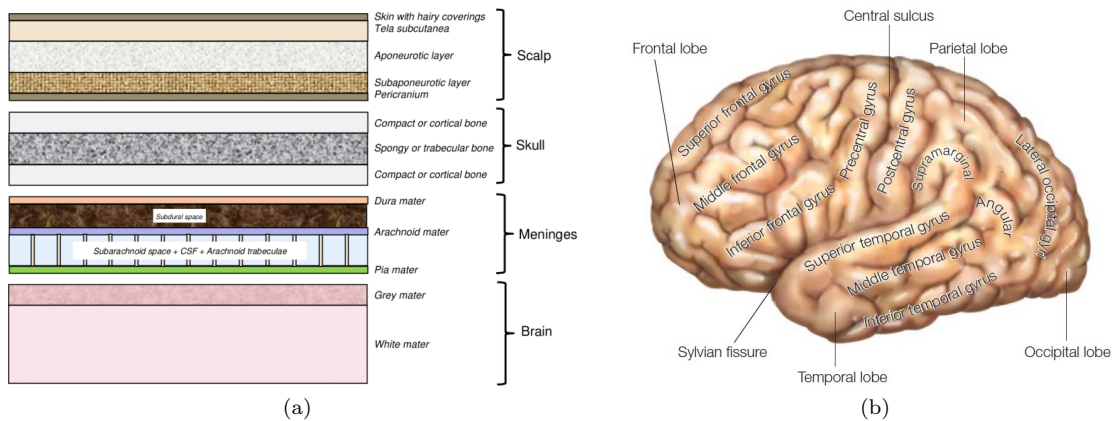


Figure 2.1: (a) Different tissues in the human head surrounding the brain.[3] (b) Different areas of the cerebral cortex.[1]

The human head is made up of different tissues with specific functions such as the protection of the brain (Skull) as can be seen in Figure 2.1a. The signals measured by an EEG are omitted in the cerebral cortex, which is the outermost layer of the brain. It ranges from 1.5 to 4.5 mm thickness and has a folded structure as can be seen in Figure 2.1b. This allows for more surface area to be packed into less head volume and also brings different areas closer together. These

areas can not only be divided optically and anatomically by sulci (the valleys of the foldings) and gyri (the crests) but also functionally as different regions serve different purposes like the primary somatosensory or the primary motor cortex.

The cortex is mostly made up of the cell bodies of neurons, which is the reason for its grayish appearance in comparison with the underlying paler tissues and motivates the term gray matter. On average, a human brain consists of 86 billion neurons of which 17 billion are located in the cortex. They are the basic units responsible for receiving information, processing it by making a “decision” and possibly passing it along to other neurons using electrochemical signaling. Their interconnectivity, location and form determine the way our brain functions.

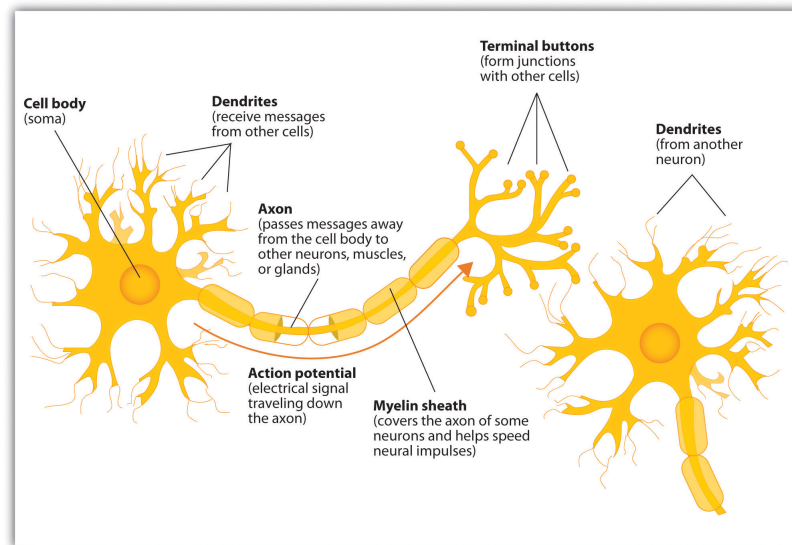


Figure 2.2: Illustration of a neuron.[4]

A neuron is composed of three main parts (Figure 2.2): The cell body (soma) contains the metabolic machinery necessary for maintaining the neuron. The dendrites are thread-like extensions responsible for receiving input from other neurons. The axon begins at the axon hillock and passes output to other neurons or different cell types. Electrical signals travel along the axon and are passed onto the next cell at the synapses via electrical or chemical transmission.

The input potentials from multiple dendrites accumulate at the axon hillock. If a certain threshold is reached, the neuron fires and a so-called action potential travels down the axon. This form of electric signalling is based on voltage-gated ion channels. Once an action potential arrives from the direction of the soma, these channels open, leading to an abrupt change in inside versus outside potential. Even though this process produces high voltage differences compared to the input potential at the dendrites it only takes about 0.5 to 2 ms and additionally, the action potentials across different neurons are not synchronized enough to add up. Because of these reasons, action potentials are not measurable with an EEG.[5, 6]

Once the action potential reaches a synapse, it is transmitted to the next neuron electrically or chemically. The potential difference between a dendrite and the corresponding soma induces an extracellular balancing flow from the soma to the dendrite and results in a dipolar electromagnetic field. The postsynaptic potential lasts for 10 to 100 ms and thus is of measurable duration. Even

though the generated potentials are small compared to that of an action potential, they occur similarly oriented and simultaneously for some ten-thousand neurons.[7] Especially patches of pyramidal cells found in the cortex generate such signals measurable with an EEG.[5, 8] We thus shift from the microscopic view of single neurons to that of an EEG, which only sees bundles of neurons from a macroscopic view and their postsynaptic potential.[9]

We conclude that for our EEG problem we are interested in dipolar sources located in the cerebral cortex.[7, 10] Source reconstruction from EEG measurements as well as the forward problem of predicting the measured potential generated by a known source is further complicated by the folded structure of the cortex as well as the different tissues with different conductivities which distort the electromagnetic field.

Chapter 3

The Finite Element Methods of DUNEuro

DUNEuro is an open-source software toolbox for bioelectromagnetic forward modeling and can be used for example to solve the EEG forward problem.[11] It makes use of Finite Element Methods (FEM) to solve a Poisson type partial differential equation for the electric potential. As FEMs are volume-based methods, they have the advantage of being able to cope with the complicated geometry of the head, e.g. the folded structure of the brain as well as with tissues with anisotropic conductivity. We focus on the classical Lagrangian Continuous Galerkin FE approaches which are implemented in DUNEuro amongst other methods. Since FEM approaches take the potential in the entire head volume into account, modeling source activity is a more intricate question compared to BEM approaches. One typically models the activity as a highly singular mathematical point dipole, and one has to take special care to properly incorporate this. Different approaches to this problem have been presented and validated in the past.

We start this chapter by developing the necessary mathematical foundation for an application of finite element methods. We use the physiological basis presented in the previous chapter and a quasi-static version of Maxwell's equation to arrive at a partial differential equation for the electric potential. This is then reformulated in a weak sense and a finite element approach is applied. Two source models used in the comparison study of DUNEuro with BEM-FMM are presented. Furthermore, the transfer matrix approach, contributing significantly to the efficiency of DUNEuro, is introduced. Finally, a few remarks about software implementation specifics are made.

3.1 A Partial Differential Equation for the Electric Potential

We would like to derive a mathematical model of the processes inside the brain described in chapter 2 and follow the well-established and widely used approach described for example in [7, 12, 2, 13]. An introduction and summary can be found in [13]. The basis of classical electromagnetism are Maxwell's equations, four coupled partial differential equations.[14] We can simplify these as propagation effects as well as capacitive and inductive effects may be neglected.[15] The quasi-static Maxwell's equations then read as follows

$$\nabla \cdot E = \frac{\rho}{\varepsilon_0} \quad (3.1)$$

$$\nabla \times E = 0 \quad (3.2)$$

$$\nabla \cdot B = 0 \quad (3.3)$$

$$\nabla \times B = \mu_0 J, \quad (3.4)$$

where E is the electric field, ρ the electric charge density, ε_0 the permittivity and μ_0 the permeability of free space, B the magnetic field and J the total electric current density. The electric field is a gradient field because of Equation 3.2, i.e. we can write $E = -\nabla u$. This simply expresses that the electric field is the gradient of the electric potential u .

As described in the previous chapter, we have an intracellular electric signal inside the dendrites, which is modelled by the so-called primary current j^p as well as a return current σE due to the electric field, where σ denotes the conductivity tensor. Thus, the total current density J is split into

$$J = j^p - \sigma \nabla u. \quad (3.5)$$

As noted before, the head is an inhomogeneous medium and the value of the conductivity tensor σ depends on the tissue it is evaluated in. Specific tissues may further be modelled as anisotropic, i.e. σ operates differently in different directions and it is a matrix instead of a scalar value.

Finally, we use Equation 3.3 to infer

$$0 = \nabla \cdot \nabla \times B = \mu_0 \nabla \cdot J = \mu_0 \nabla \cdot (j^p - \sigma \nabla u), \quad (3.6)$$

which we can rewrite as

$$\nabla \cdot \sigma \nabla u = \nabla \cdot j^p. \quad (3.7)$$

Plonsey and Heppner have further shown in [15], that the normal current density $\langle J, n \rangle$, where n denotes the unit outer normal, is continuous across boundaries between tissues. That is, if E_1 and E_2 are the electric fields inside and outside of the boundary with regard to the normal vector n and σ_1, σ_2 the corresponding conductivities, we have

$$\langle \sigma_1 E_1, n \rangle = \langle \sigma_2 E_2, n \rangle. \quad (3.8)$$

At the head surface the outer medium is air which (nearly) has zero conductivity. At the head surface we thus end up with the condition

$$\langle \sigma E, n \rangle = 0. \quad (3.9)$$

Let us summarize the resulting PDE model of our problem.

Definition 3.1.1 (DUNEuro EEG forward problem). *Let us denote the head domain by Ω and its boundary, the head surface, by $\Gamma = \partial\Omega$. Let further u be the electric potential, σ the conductivity and j^p the primary current due to neural activity. The following partial differential equation with Neumann boundary condition then needs to be solved for the potential u .*

$$\begin{aligned} \nabla \cdot \sigma \nabla u &= \nabla \cdot j^p && \text{in } \Omega \\ \langle \sigma \nabla u, n \rangle &= 0 && \text{on } \Gamma, \end{aligned} \quad (3.10)$$

where n is the unit outer normal.

It is further common to approximate the primary current j^p as a superposition of mathematical point dipoles.[10]

Definition 3.1.2 (Mathematical point dipole). *The primary current j^p can be modelled by*

$$j^p = M \delta_{x_0}, \quad (3.11)$$

where δ_{x_0} is the Dirac delta distribution for the position of the source x_0 and M is called the dipole moment. It is a vector modelling direction and strength of the current.

Of course this definition raises the problem that such a j^p can not be differentiated, at least not in the classical sense, and the right hand side of Equation 3.10 is not mathematically well-defined. Let us therefore for now look at $\nabla \cdot j^p$ as an abstract term for the source denoted by f which will be specified in chapter 3.4 when different source models are presented.

3.2 A Weak Formulation

We would like to solve the EEG forward problem for a given source as presented in Definition 3.1.1. Unfortunately, classical solutions, e.g. solutions u in $C^2(\Omega)$ can not exist as for example σ can not even be assumed to be continuous. The conductivity rather “jumps” between tissues as is the case at the boundary between the highly conducting cerebrospinal fluid (CSF) and the isolating skull.[16] Instead, we formulate a weak version of our problem (see e.g. [17]). This also leads to a natural way to actually compute approximations of solutions as we will see.

The weak formulation is motivated by the fundamental lemma of the calculus of variations. We multiply the PDE from Definition 3.1.1 with a function v from a test function space H which we will choose later and integrate over the head domain Ω

$$\int_{\Omega} (\nabla \cdot \sigma \nabla u) v \, dx = \int_{\Omega} f v \, dx. \quad (3.12)$$

Now we use integration by parts to arrive at

$$\int_{\Omega} (\nabla \cdot \sigma \nabla u) v \, dx = - \int_{\Omega} \langle \sigma \nabla u, \nabla v \rangle \, dx + \int_{\Gamma} \langle \sigma \nabla u, n \rangle v \, dx. \quad (3.13)$$

As the second term vanishes because of the zero Neumann boundary condition, we can define the weak formulation as follows.

Definition 3.2.1 (Weak formulation of the DUNEuro EEG forward problem). *We would like to find an $u \in H^1(\Omega)$, s.t.*

$$\int_{\Omega} \langle \sigma \nabla u, \nabla v \rangle dx = \int_{\Omega} -fv dx \quad \text{for all } v \in H^1(\Omega). \quad (3.14)$$

Defining

$$a(u, v) = \int_{\Omega} \langle \sigma \nabla u, \nabla v \rangle dx \quad (3.15)$$

$$l(v) = \int_{\Omega} -fv dx, \quad (3.16)$$

this can be written as $a(u, v) = l(v)$ for all $v \in H^1(\Omega)$.

Here, $H^1(\Omega)$ denotes the Sobolev space (see [18]). This choice of H is a common approach, see for example [19, 17].

Note that only l depends on our choice of model for the source. It is useful to look at l simply as a linear functional on $H^1(\Omega)$. We will later see different approximations of this source term in chapter 3.4. For the next result it is only important that l is continuous which we will assume from now on.

Theorem 3.2.2. *Let a be as in Definition 3.2.1 and $H_*^1(\Omega)$ be defined as all Sobolev functions with zero mean, that is*

$$H_*^1(\Omega) = \{v \in H^1(\Omega) \mid \int_{\Omega} v dx = 0\}. \quad (3.17)$$

Provided that Ω fulfills some conditions and l is continuous, the problem

$$a(u, v) = l(v) \quad \text{for all } v \in H_*^1(\Omega) \quad (3.18)$$

has exactly one solution. Furthermore, this solution fulfills Equation 3.18 for all $v \in H^1(\Omega)$.

For a full proof using standard techniques for variational problems please refer to [17]. For the existence and uniqueness of a solution u we had to restrict our search space $H^1(\Omega)$ to those Sobolev functions with zero mean. This actually reflects real properties of the EEG as a reference electrode has to be chosen. Different reference electrodes (real or abstract like the common average reference) lead to a shift of the measured potential by a constant. By requiring zero mean one baseline is chosen. The following Lemma formulates this mathematically (see [20]).

Lemma 3.2.3. *There exists some $u_0 \in H_*^1(\Omega)$, such that the set of solutions in $H^1(\Omega)$ of*

$$a(u, v) = l(v) \quad \text{for all } v \in H^1(\Omega), \quad (3.19)$$

is of the form $u_0 + \mathbb{R} \cdot 1$.

3.3 The Finite Element Method

Now that we have established a formulation of our problem which has a solution, the question remains how to actually numerically compute it remains. One widely used approach in fields like electromagnetism and engineering is the finite element method (FEM). For details see for example [21].

The basic mathematical idea is as follows. The space H , in our case $H^1(\Omega)$, is infinite-dimensional. We can try to approximate a solution in H by moving to a finite-dimensional subspace $V \subset H$ and search for a $u \in V$ satisfying

$$a(u, v) = l(v) \quad \text{for all } v \in V. \quad (3.20)$$

There also exist approaches where the ansatz function u and the test functions v are from different spaces, but we will work with $u, v \in V$. As V is a finite-dimensional linear space we can find a basis $\{\varphi_1, \dots, \varphi_n\}$ and because a is bilinear and l is linear, we see that our problem in V is equivalent to solving

$$a(u, \varphi_i) = l(\varphi_i) \quad \text{for all } 1 \leq i \leq n. \quad (3.21)$$

Now as we search for $u \in V$, we can represent u as a linear combination of the basis $u = \sum_{j=1}^n x_j \varphi_j$ and the above equation reads as

$$\sum_{j=1}^n x_j a(\varphi_j, \varphi_i) = l(\varphi_i). \quad (3.22)$$

We summarize this as

Lemma 3.3.1. *Let A be defined by $A_{ij} = a(\varphi_j, \varphi_i)$ and b by $b_i = l(\varphi_i)$. Then solving the linear problem*

$$Ax = b \quad (3.23)$$

is equivalent to solving the problem described in Definition 3.2.1 in V via the identification $x \mapsto \sum_{j=1}^n x_j \varphi_j$.

The matrix A is often called the stiffness matrix. The usual way to choose the finite-dimensional subspace V is to split the domain Ω into subdomains and then use functions which are computationally easy to handle on these subdomains. This idea is the finite element method (FEM). An application of FEM to the forward problem has been discussed for example in [22].

As we have seen in Lemma 3.2.3, the arbitrary choice of a reference electrode is reflected in the set of solutions in $H^1(\Omega)$. This extends to finite-dimensional subspaces as has been shown in [20].

Theorem 3.3.2. *Let $V \subset H^1(\Omega)$ be a finite-dimensional linear subspace with basis $\varphi_1, \dots, \varphi_n$ and $\sum_{j=1}^n \varphi_j = 1 \in V$. Then the set of solutions $u \in V$ for the problem*

$$a(u, v) = l(v) \quad \text{for all } v \in V \quad (3.24)$$

is of the form $u_0 + \mathbb{R} \cdot 1$ for some $u_0 \in V$. Considering the equivalent problem $Ax = b$, the solution space is of the form $x_0 + \mathbb{R} \cdot \begin{pmatrix} 1 \\ \vdots \\ 1 \end{pmatrix}$.

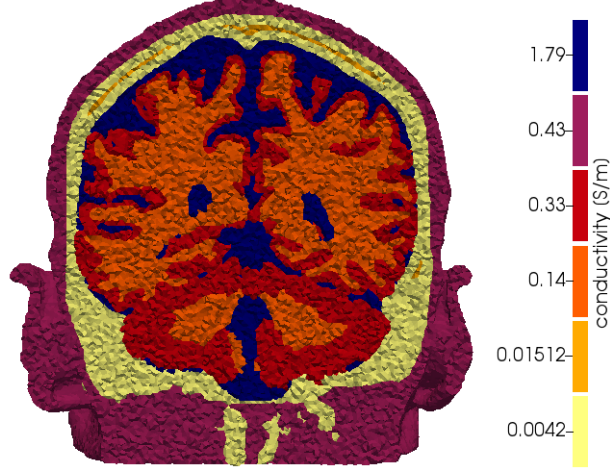


Figure 3.1: Tetrahedral mesh of a realistic head model.[23]

Let us now look at a commonly used example for finite-dimensional subspaces. As mentioned, we split the head domain into subdomains which must fulfill certain properties (see [21]). In our case, we represent Ω as the union of non-overlapping three-dimensional simplices, i.e. tetrahedra (see Figure 3.1). Each tetrahedron is defined solely by its four corner points, the vertices. Let τ be one such mesh of the head. One easy to handle but effective subspace is then given by the continuous functions which are linear on each tetrahedron.

$$V_\tau = \{v \in C^0(\Omega) | v|_T \in P^1(T) \text{ for all } T \in \tau\}. \quad (3.25)$$

If y_1, \dots, y_n are all vertices of all tetrahedra contained in τ , then a basis of V_τ is given by the functions $\varphi_1, \dots, \varphi_n$ which fulfill

$$\varphi_j(y_i) = \begin{cases} 1 & , \text{ if } i = j \\ 0 & , \text{ if } i \neq j \end{cases}. \quad (3.26)$$

These functions are called the Lagrange basis (for details see [21]). Of course there exist other choices of V which have been implemented and tested for our application in bioelectromagnetism. Different types of meshes, e.g. hexahedral meshes, have been used in [17]. An approach with discontinuous functions has been investigated in [24] and higher order polynomials have been compared as well[25].

We will focus on the above space presented in Equation 3.25. A nice property of the basis functions is that because of

$$u(y_i) = \sum_{j=1}^n x_j \varphi_j(y_i) = x_i, \quad (3.27)$$

the coefficients representing any function $u \in V_\tau$ are simply the evaluations of u at the vertices y_1, \dots, y_n .

The next step in our effort to solve the forward problem now is to find a solution for the linear system $Ax = b$. A popular classic iterative solver is the (preconditioned) conjugate gradient method (PCG) as presented in the context of FEM for example in [21]. Unfortunately, Theorem 3.3.2 illustrates that the stiffness matrix A can not be positive definite as its null space is not trivial. We could restrict V to functions from $H_*^1(\Omega)$ to achieve uniqueness similar to Theorem 3.2.2, but this does not seem practical as we destroy nice properties of our space of linear functions and its basis. An interesting discussion about this problem and several ways to solve it can be found in [20]. For us it suffices to state Theorem 3.3.3.

Theorem 3.3.3. *Let A be the stiffness matrix and b the right hand side vector as defined above. If we then set*

$$\hat{A} = \begin{pmatrix} 1 & 0 & \dots & 0 \\ 0 & a_{22} & \dots & a_{2m} \\ \vdots & \vdots & \ddots & \vdots \\ 0 & a_{m2} & \dots & a_{mm} \end{pmatrix} \quad (3.28)$$

and

$$\hat{b} = \begin{pmatrix} 0 \\ b_2 \\ \vdots \\ b_m \end{pmatrix}, \quad (3.29)$$

the matrix \hat{A} is symmetric positive definite and the solution of $\hat{A}x = \hat{b}$ is the unique solution of $Ax = b$ where the first entry of x is zero.

Of course the choice of index $1 \leq i \leq n$, in our case $i = 1$, for altering A to \hat{A} and b to \hat{b} is arbitrary and the above holds for any i . We also recall that with our choice of ansatz functions and basis, we have $x_i = u(y_i)$. We thus look for the unique solution with $u(y_1) = 0$.

A software implementing this numerical approach has to compute the stiffness matrix A (or the very similar \hat{A}) or its operation Ax on a vector. Common basis functions are tied to the elements which divide the domain. This is done in a manner similar to the Lagrange basis and the functions have only limited support. Thus the term

$$A_{ij} = a(\varphi_j, \varphi_i) = \int_{\Omega} \langle \sigma \nabla \varphi_j, \nabla \varphi_i \rangle dx \quad (3.30)$$

vanishes for most $1 \leq i, j \leq n$. The support of a Lagrange basis function φ_i for example is exactly the tetrahedra which have the node x_i as a vertex. Thus the stiffness matrix is very sparse. The above involves the task of integration but we do not need to integrate arbitrary functions. The a-priori knowledge of the basis functions allows for a clever, exact implementation. The gradients of the Lagrange basis for example are constant on each tetrahedron as the functions themselves are linear. Furthermore, the partition of the domain into the elements T leads to a natural decomposition of the integral $\int_{\Omega} \cdot dx = \sum_{T \in \tau} \int_T \cdot dx$.

We have now outlined a way to reach a formulation that can actually be implemented and solved numerically. In an application, we would first have to generate the relevant data for the head of the person in question. For this purpose, a magnetic resonance imaging (MRI) scanner is used and the result is segmented into the different tissues. Conductivities are assigned to each tissue

and the head model is meshed, e.g. into tetrahedra. The positions of the electrodes have to be registered as well. A more detailed description of this process can be found for example in [26] and the resulting data set under [27].

A solver now has to set up and solve the linear system resulting from the given mesh, its conductivities, the electrodes and the choice of basis functions. Another parameter we will look at is the choice of source model which determines the way the vector b is computed.

3.4 Source Models

There are different approaches on how to model a dipolar source and thus on how to compute the linear functional l . These models differ with respect to the quality of the subsequent solutions u , that is the approximation error, as well as computational speed, sensibility for the eccentricity of the sources, i.e. how close they are to a tissue boundary with a conductivity jump and their behavior regarding different, complicated head geometries and meshes.

In the following, we will present the partial integration and the Saint Venant approaches. Further models include the Subtraction approach[28, 17, 22] and variations of it. This is a classical model that has been examined deeply and is mathematically well understood. Other source models can be found in [19, 29, 30].

These two models were chosen as they are a good representation of fast and easy as well as somewhat slower but more precise FEM source models. While the computation effort for the source term b is low with the partial integration approach, the Venant approach produces better results at the cost of higher computational intensity[31, 5, 30].

3.4.1 The Partial Integration Model

The partial integration approach is also referred to as a direct FE approach as we simply extend our FE method from the left-hand side of the weak formulation to the right-hand side. It is thus canonical and easy to derive as well as simple and quickly to compute as we will see. Downsides can be seen in the quality of the solutions in comparison to other models. More about the partial integration model can be found in [32, 33, 34, 28].

We had determined the right-hand side of the weak formulation as

$$l(v) = \int_{\Omega} -(\nabla \cdot j^p)v \, dx. \quad (3.31)$$

Integration by parts yields

$$l(v) = \int_{\Omega} \langle j^p, \nabla v \rangle \, dx + \int_{\Gamma} \langle j^p, n \rangle v \, d\Gamma \quad (3.32)$$

and as the source term vanishes on the head surface we arrive at

$$l(v) = \int_{\Omega} \langle j^p, \nabla v \rangle \, dx. \quad (3.33)$$

Modeling j^p as a mathematical point dipole $M\delta_{x_0}$ (see Definition 3.1.2), we finally have

$$l(v) = \langle M, \nabla v(x_0) \rangle. \quad (3.34)$$

Using our basis functions $\varphi_1, \dots, \varphi_n$, this reads as follows.

Definition 3.4.1 (partial integration model). *If we have a source at location x_0 with an orientation and strength of M , the partial integration approach models the right-hand side vector b as*

$$b_i = l(\varphi_i) = \langle M, \nabla \varphi_i(x_0) \rangle. \quad (3.35)$$

With our choice of ansatz space and basis, the term $\nabla \varphi_i$ can be computed easily as it is element-wise constant and additionally vanishes on all tetrahedra which do not have y_i as a vertex. Thus we only need to determine the tetrahedron containing our source x_0 and compute all b_i belonging to nodes y_i that are vertices of that tetrahedron. All other entries of b are zero and the right-hand side vector is very sparse. We also note that as long as the source x_0 is contained in the same tetrahedron, the source term b does not vary and the forward problem solution using this model is constant. The results are optimal at the tetrahedron barycenter.[30]

3.4.2 The Saint Venant Model

This model avoids the dipolar source by using a monopole distribution. The monopoles must of course maintain certain properties of the original source which are to be discussed. Applied to the problem at hand, the Principle of Saint Venant then states that from “far away”, i.e. at the electrodes, these two source terms can be assumed to be equivalent. The original Venant approach was first presented in [35] and was named the “blurred dipole approach”. Different alterations of it have since been derived, some of which we will see in the following.

Let us first discuss the choice of the monopole locations before discussing their loads. As we make use of FEM and thus have a mesh of the head geometry at hand, it is canonical and common to choose as first monopole location y_{j_1} the mesh vertex closest to the dipole location x_0 . We then further choose all vertices y_{j_2}, \dots, y_{j_l} which are directly connected to y_{j_1} by an edge, i.e. lie in one same mesh element as y_{j_1} . It has been shown[36], that only those mesh vertices are suitable, that are in the same tissue compartment as the source x_0 , the so-called Venant condition.

If we denote the loads corresponding to y_{j_1}, \dots, y_{j_l} by q_1, \dots, q_l , the source term f used in Theorem 3.2.1 is given by

$$\sum_{i=1}^l q_i \delta_{y_{j_i}}. \quad (3.36)$$

If we apply the resulting linear functional l to the Lagrange basis, we see that $b_i = -q_i$, if i is one of the indices j_1, \dots, j_l and b_i is zero otherwise. Given a monopole distribution with loads, the right-hand side vector b is thus easy to compute and very sparse.

We are left with the problem of determining the strengths q_i of the monopoles. As we would like to approximate our validated model of a dipolar source, the idea is to compute the moments of both the given dipolar source and the monopolar approximation and try to choose q_i so that they equal. By reproducing the moments we aim at approximating the potential generated by a point dipole as accurately as possible. There are different approaches on how these moments are chosen.

The original Saint Venant model[35], in later publications referred to as the monopolar Venant model, defines the s -th moment of the monopole distribution as

$$\sum_{i=1}^l q_i (y_{j_i} - x_0)^s. \quad (3.37)$$

The exponent has to be understood as a pointwise operation in this context. Now the second moment of the dipolar source is simply the magnitude vector M , all other moments are zero. Thus we get three linear equations for the vector q of monopole loads for each moment $s \geq 1$, one for each dimension. It is common to use the first three moments $s = 0, 1, 2$.

In order to improve the condition of this problem it is common to scale all positions by a reference length. Then, Tikhonov regularization is used in order to ensure uniqueness of the solution. This regularization is chosen so that it penalizes terms with a high spatial frequency. It ensures smoothness for the monopoles. Additionally, large absolute loads $|q_i|$ are avoided as these usually are blind sources which do not contribute to the far-field.[37]

The multipolar Venant approach on the other hand makes use of the definition of multipole expansion as used in physics.[38, 39, 40] The idea can be roughly summarized as follows. In a homogeneous medium, the potential evoked by a dipolar source as well as by a monopolar source distribution is known analytically. As we can assume that there exists a small homogeneous region around the source locations, we would like both of these resulting potentials to be equal. We can write them as a multipole expansion and set a certain number, usually three, of these expansion terms, i.e. the moments, to be equal. This leads to a linear system of equations where the terms for the first two moments are the same as in Equation 3.37 but the second order moment differs. Once again, the above Tikhonov regularization term is added.

Nüßing presents a more general framework[37] in which both of these approaches can be formulated. This leads to further possibilities, for example mixed moments can be included in the same form as in Equation 3.37 by replacing the exponent s by a multiindex α . Thus, we are not limited to pointwise operations but have moments which link the three dimensions of the terms $y_{j_i} - x_0$. Furthermore, quadrupolar moments arranged in patches have been examined in [38].

3.5 The Transfer Matrix Approach

Applications of the forward problem require solutions for test sources at many different locations. For example approaches to the inverse problem (e.g. hierarchical Bayesian inference[41]), that is locating the source of measured neural activity, rely on a so-called lead-field matrix containing as columns the predicted measurements at the electrodes for thousands or even tens of thousands sources. We see that simply solving the forward problem accurately does not suffice. A useful solver needs to be able to do so for a great number of sources in an acceptable time on computing architectures commonly found in a research but also a clinical environment. The transfer matrix approach tackles this difficulty and was introduced for example in [42].

The mathematical concept behind it can be paraphrased by and is based on the simple observation that we are not really interested in a solution potential u in the whole head domain Ω but would only like to know its value at the electrode positions. Let z_1, \dots, z_m be the electrode positions and $u = \sum_{i=1}^n x_i \varphi_i$ the solution of the linear problem stated in Theorem 3.3.3. We then look for the electrode potential vector V with

$$V_j = u(z_j) = \sum_{i=1}^n x_i \varphi_i(z_j). \quad (3.38)$$

If we then require a certain electrode, say the electrode located at z_1 , to be the reference electrode, we do a baseline correction by subtracting the potential at z_1 . We now have

$$V_j = u(z_j) - u(z_1) = \sum_{i=1}^n x_i \varphi_i(z_j) - \sum_{i=1}^n x_i \varphi_i(z_1) = \sum_{i=1}^n x_i (\varphi_i(z_j) - \varphi_i(z_1)). \quad (3.39)$$

Defining the matrix R as $R_{ji} = \varphi_i(z_j) - \varphi_i(z_1)$, the above can be written as $V = Rx$. Evaluating the solution only at the electrodes is thus a linear map applied on our FEM solution x . Combining the linear problem and this linear operator, we see that

$$V = Rx = R\hat{A}^{-1}\hat{b}. \quad (3.40)$$

Defining $T = R\hat{A}^{-1}$, solving the forward problem for many different sources now reduces to two inexpensive steps. Per source, we set up the right-hand side \hat{b} and simply apply the linear operator T .

Of course, the computation of T now poses the real difficulty. Direct computation is numerically unfeasible. We rather see that

$$\hat{A}T^t = (T\hat{A})^t = R^t. \quad (3.41)$$

As \hat{A} is simply the stiffness matrix and R^t can be computed as defined above, we have derived linear equations for the columns of T^t which are the rows of T . Let us summarize this result.

Theorem 3.5.1 (Transfer matrix). *Let us define R by $R_{ji} = \varphi_i(z_j) - \varphi_i(z_1)$, where z_1, \dots, z_m are the electrode positions. We can solve*

$$\hat{A}T^t = R^t, \quad (3.42)$$

column-wise in order to find the rows of the transfer matrix T . If $\hat{b}_1, \dots, \hat{b}_k$ are the right-hand sides for k sources, we can compute the resulting potential at the electrodes simply by applying

$$V_j = T\hat{b}_j, \quad (3.43)$$

for $1 \leq j \leq k$.

Similar to the computation of the stiffness matrix, we note that the matrix R is easy to determine and sparse because of the limited support and the a-priori knowledge of the basis functions.

The advantage of the transfer matrix approach now is the following. The main computational effort, solving linear systems, has been shifted from the sources to the electrodes. Instead of solving a linear system for each source, we only have to solve a linear system per non-reference electrode. The effort of assembling the matrix R and applying the resulting linear operator for each source is fast in execution. Typical use cases involve thousands of sources, but a common electrode cap only has around 75 electrodes[43, 44].

3.6 DUNEuro

All of the numerical theory presented in this chapter and more has been realized in the C++ software toolbox DUNEuro for bioelectromagnetic forward modeling.[11] DUNEuro also provides interfaces to Python and MATLAB for ease of use.

It is based on DUNE, the Distributed and Unified Numerics Environment.[45] This general purpose and open-source C++ library is a toolbox for solving partial differential equations with mesh-based methods. It links each mesh element to a reference element using affine maps and provides easy access to the basis functions, their gradients, quadrature rules and more.

At the heart of our FEM approach lay linear equations that need to be solved. A vast number of highly developed algorithms for such problems are accessible. These state-of-the-art linear solvers like CG, GMRES or BiCGSTAB and preconditioners such as SSOR, incomplete Cholesky or the AMG allow for an efficient and precise computation of the sought solutions. Additional speed has been gained using the newly implemented block krylov methods in combination with the transfer matrix approach.[20] DUNEuro further makes use of parallelization and is thus fit for application on high performance workstations.

Chapter 4

The Boundary Element Fast Multipole Method

A boundary element method (BEM) consists of a formulation of a problem on surfaces instead of a volume, commonly the boundaries of the volume in question. This formulation is then solved similarly to the above chapter 3.3 by using a finite dimensional ansatz space and reducing the equation at hand to a system of linear equations. At the core of the BEM-FMM idea sits the Fast Multipole Method (FMM) which efficiently computes electromagnetic particle interaction. BEM-FMM has been used mostly in non-medical fields such as in the context of defense[46, 47] and in high-frequency electromagnetics[48, 49]. There also have been attempts to apply FMM to the forward problem[13, 50, 51, 52], but they did not seem to generate convincing results and were not followed further. The approach we present here and compare later on seems to be the first application of BEM-FMM of this kind to the quasistatic bioelectromagnetism forward problem and has been described in [53, 54, 55, 56, 57].

First, we follow the physiological and physical basis presented at the beginning and the theory already established in the chapter on the finite element methods of DUNEuro in order to derive integral equations for the electric surface charge distribution ρ . In contrast to the last chapter, we do not solve for the potential directly but instead solve for ρ . Two approaches are presented. One direct approach which models the source via primary and secondary electric potential and field. The second approach makes use of electrode stimulation and links this problem to the forward problem by Helmholtz reciprocity. Next, we explain how the integral equations for both approaches can be discretized to a linear system with a Galerkin approach. Finally, computational details are described. We see how the fast multipole method is used to greatly reduce computational effort and form a matrix-free operator for the dense system matrix resulting from the integral equations. Also, more exact integration is presented for sources and targets which are too close for the FMM and further implementation details are given.

4.1 Integral Equations for the Electric Surface Charge Distribution

We are working with the same physiological and physical basis as in chapter 2 and chapter 3.1 and can thus once more consider electromagnetics in a quasi-static context for our effort to model the connection between cortical source and EEG recordings in order to solve the forward problem.

Instead of investigating the electric potential directly, we look at induced electric surface charges with a density ρ residing on tissue boundaries with an abrupt conductivity change. These surface charges are due to e.g. the dipolar source. Let us denote the surfaces in question by S . If the density ρ is given Coulomb's law determines the resulting electric potential up to a constant and the electric field at a point $r \notin S$ as

$$\begin{aligned}\varphi(r) &= \int_S \frac{1}{4\pi\epsilon_0} \frac{\rho(r')}{|r - r'|} dr' \\ E(r) &= \int_S \frac{1}{4\pi\epsilon_0} \frac{\rho(r')(r - r')}{|r - r'|^3} dr'.\end{aligned}\tag{4.1}$$

Here, ϵ_0 is the dielectric permittivity of vacuum. Even though we are interested in the potential measured at the electrodes, it thus suffices to solve for the surface charge density in order to compute its effect.

There are two related ways to proceed and derive a model for ρ . The following, more direct and canonical approach, actually takes the source into consideration in the form of a primary electric field.

4.1.1 Modeling the Source Directly

This derivation follows the theory explained in [56].

As illustrated in Figure 4.1, a cortical dipole evokes a primary electric field E^p . This induces surface charges which accumulate on tissue boundaries which in turn create a secondary electric field E^s . Our goal is to find the surface charge density enabling us to apply Coulomb's law in order to compute E^s and thus $E = E^p + E^s$ and the potentials φ^s and $\varphi = \varphi^p + \varphi^s$, respectively.

A condition that is central in deriving a suitable equation for ρ is local current continuity at conductivity boundaries, also called Kirchhoff's current law. We have seen this statement before in Equation 3.8 and repeat it here for convenience. For $r \in S$ it states that

$$\langle \sigma_{\text{in}}(r)E_{\text{in}}(r), n(r) \rangle = \langle \sigma_{\text{out}}(r)E_{\text{out}}(r), n(r) \rangle\tag{4.2}$$

with E_{in} being the field just inside the boundary and E_{out} the field just outside. $\sigma_{\text{in}}, \sigma_{\text{out}}$ are the corresponding conductivities and n is the outer normal vector (see Figure 4.2). Let us be more precise and define $E_{\text{in}}, E_{\text{out}}$ via limits as

$$E_{\text{in/out}}(r) = \lim_{h \rightarrow 0} E(r \mp hn(r)).\tag{4.3}$$

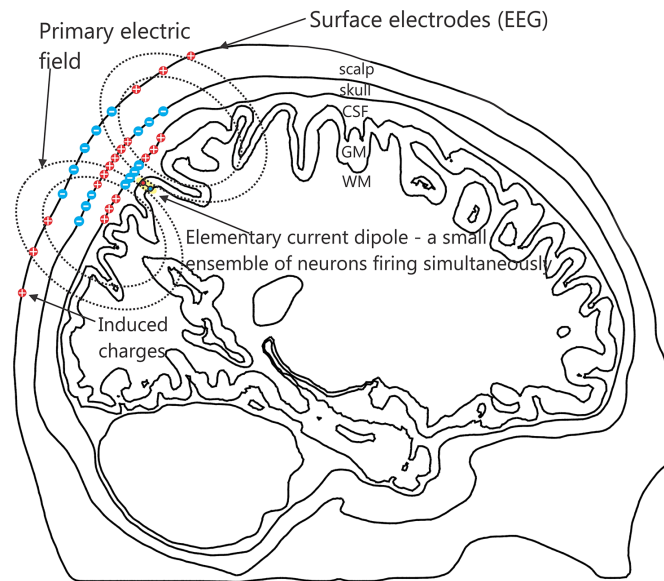


Figure 4.1: Illustration of the electric surface charges induced by a cortical source[56]

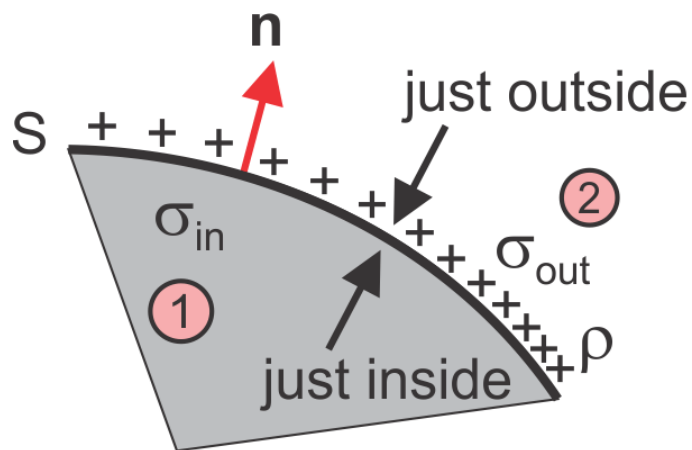


Figure 4.2: Electric surface charges at a tissue conductivity boundary.[56]

Next, we can plug in

$$E(r) = E^p(r) + E^s(r) = E^p(r) + \int_S \frac{1}{4\pi\epsilon_0} \frac{\rho(r')(r-r')}{|r-r'|^3} dr'. \quad (4.4)$$

While the primary electric field is continuous at the boundaries, the secondary is not and its limit from in- and outside can be derived as shown in [58]. We then have

$$E_{\text{in}}(r) = E^p(r) + \lim_{\epsilon \rightarrow 0} \int_{S \setminus B_\epsilon(r)} \frac{1}{4\pi\epsilon_0} \frac{\rho(r')(r-r')}{|r-r'|^3} dr' - \frac{1}{2\epsilon_0} \rho(r)n(r). \quad (4.5)$$

Let us denote the improper integral simply as $\int_S \cdot dr'$ in the following. Proceeding similarly for E_{out} Equation 4.2 then states that

$$\begin{aligned} & \langle \sigma_{\text{in}}(r) \left(E^p(r) + \int_S \frac{1}{4\pi\epsilon_0} \frac{\rho(r')(r-r')}{|r-r'|^3} dr' - \frac{1}{2\epsilon_0} \rho(r)n(r) \right), n(r) \rangle = \\ & \langle \sigma_{\text{out}}(r) \left(E^p(r) + \int_S \frac{1}{4\pi\epsilon_0} \frac{\rho(r')(r-r')}{|r-r'|^3} dr' + \frac{1}{2\epsilon_0} \rho(r)n(r) \right), n(r) \rangle \end{aligned} \quad (4.6)$$

for $r \in S$. We can reorder this as

$$\begin{aligned} (\sigma_{\text{in}} + \sigma_{\text{out}}) \frac{1}{2\epsilon_0} \rho(r) - \langle (\sigma_{\text{in}} - \sigma_{\text{out}}) \int_S \frac{1}{4\pi\epsilon_0} \frac{\rho(r')(r-r')}{|r-r'|^3} dr', n(r) \rangle \\ = \langle (\sigma_{\text{in}} - \sigma_{\text{out}}) E^p(r), n(r) \rangle. \end{aligned} \quad (4.7)$$

Multiplying by 2 and dividing by $\sigma_{\text{in}} + \sigma_{\text{out}}$, we finally have to the equation

$$\frac{1}{\epsilon_0} \rho(r) - 2 \frac{\sigma_{\text{in}} - \sigma_{\text{out}}}{\sigma_{\text{in}} + \sigma_{\text{out}}} \langle \int_S \frac{1}{4\pi\epsilon_0} \frac{\rho(r')(r-r')}{|r-r'|^3} dr', n(r) \rangle = 2 \frac{\sigma_{\text{in}} - \sigma_{\text{out}}}{\sigma_{\text{in}} + \sigma_{\text{out}}} \langle E^p(r), n(r) \rangle. \quad (4.8)$$

We define K as the electric conductivity contrast $\frac{\sigma_{\text{in}} - \sigma_{\text{out}}}{\sigma_{\text{in}} + \sigma_{\text{out}}}$. Note that K does depend on the point of evaluation $r \in S$ but is constant per tissue interface.

We may replace our variable of interest and solve for $\frac{\rho}{\epsilon_0}$ instead. This eliminates ϵ_0 in the above equation. As Coulomb's law (Equation 4.1) also involves $\frac{\rho}{\epsilon_0}$ and the resulting potential or field is what we are really interested in, this allows us to avoid dealing with ϵ_0 at all. In the following definition we will use the letter ρ , even though one has to keep in mind that the permittivity is missing.

Definition 4.1.1 (BEM-FMM integral equation with primary field). *We are interested in finding an electric charge distribution ρ which fulfills the integral equation*

$$\rho(r) - 2K \langle \int_S \frac{1}{4\pi} \frac{\rho(r')(r-r')}{|r-r'|^3} dr', n(r) \rangle = 2K \langle E^p(r), n(r) \rangle. \quad (4.9)$$

This has previously been formulated in [59], but has been first put to practical use in the context it is presented in here. Note that only the term involving the primary electric field depends on the source. Looking back at chapter 3 and the effort of inventing the transfer matrix approach (chapter 3.5) we see that once again, a solution of the above would be linked to a particular source and we would have to solve for each source rendering it unfeasible for certain applications of the forward problem.

We need to find a suitable source model of the primary electric field E^p . This has been described in the supplement of [55].

Definition 4.1.2 (BEM-FMM primary field). *Given a dipole with small extend and current source at x_0 of strength I_0 and current sink at x'_0 of strength $-I_0$ we can derive the electric potential and field.[60] If the surrounding medium has a conductivity of σ , they are given by*

$$\begin{aligned}\varphi^p(r) &= \frac{I_0}{4\pi\sigma|r-x_0|} - \frac{I_0}{4\pi\sigma|r-x'_0|} \\ E^p(r) &= \frac{I_0|r-x_0|}{4\pi\sigma|r-x_0|^3} - \frac{I_0|r-x'_0|}{4\pi\sigma|r-x'_0|^3}.\end{aligned}\tag{4.10}$$

The moment M of such a dipole is then given by

$$M = I_0|x_0 - x'_0|.\tag{4.11}$$

In order to solve a forward problem we would now have to solve the problem stated in Definition 4.1.1 for the primary field from Definition 4.1.2. The resulting charge density ρ could then be used in order to derive the secondary potential at specific evaluation points, e.g. electrodes, by Coulomb's law (Equation 4.1). Together with the primary potential φ^p we then have our solution of the forward problem.

4.1.2 Helmholtz Reciprocity – Modeling Electrode Stimulation

Let us now think about a different question. If two electrodes located at the head surface are used to stimulate the human brain and thus apply a current instead of measuring brain activity, what is the generated electric field? This problem can be related to the forward problem of EEG via the Helmholtz reciprocity principle first stated by Hermann von Helmholtz in 1853.[61] This recent approach for BEM-FMM is described in [53]. We follow the elaborations of the aforementioned paper.

An application of this duality principle to the bioelectromagnetic problem at hand has been described in [62]. It states that if given a dipolar source at x_0 with moment M and an electrode pair located at z_1 and z_2 , respectively, we may consider the following in order to find the potential difference V between the electrodes. Assume a different setting where the source is deactivated and a current I is introduced through the electrodes, the first acting as a source while the second is a sink. It suffices to find the electric field at the dipole location $E(x_0)$ resulting from this electrode stimulation and we can apply the equation

$$V = -\frac{\langle E(x_0), M \rangle}{I}.\tag{4.12}$$

The core problem is now independent of a specific dipole. Find the electric field inside the head resulting from electrode stimulation with a current I . Computation of the actual forward problem

solution for a specific dipole is then reduced to evaluation of this field and a three-dimensional inner product. Of course the stimulation problem needs to be solved for many electrode pairs. If the electrode locations are given by z_1, \dots, z_n , we can specify z_1 as the reference electrode and $n - 1$ electrode pairs with z_1 remain. Thus, the core computational effort has been once more reduced from the number of sources to the number of non-reference electrodes, just like in chapter 3.5.

As opposed to chapter 4.1.1, we are now investigating surface charges on interfaces induced by electromagnetic stimulation. There are two kinds of surfaces which make up S . The first is the tissue conductivity boundaries S_c and the second is the electrode surfaces S_e themselves as we model them as having a small extent. Our goal is once more to determine the charge density ρ . We can then compute the electric field at the dipole locations needed for the reciprocity principle (Equation 4.12) by making use of Coulomb's law on $S = S_c \cup S_e$ (Equation 4.1).

No division into primary and secondary field is necessary here. Analogous to the previous model in chapter 4.1.1 we use Kirchhoff's local current continuity law (Equation 4.2) and define the electric field just in- and outside of an intersection as limits. Combining these terms and defining K as the electric conductivity contrast, we end up with a similar equation only missing the primary electric field term. We can avoid ε_0 and arrive at the following problem at the tissue boundaries $S_c \subset S$.

Definition 4.1.3 (BEM-FMM integral equation without primary field). *We model current continuity at the tissue boundaries by the equation*

$$\rho(r) - 2K < \int_S \frac{1}{4\pi} \frac{\rho(r')(r - r')}{|r - r'|^3} dr', n(r) > = 0, \quad (4.13)$$

for $r \in S_c$.

Furthermore, we have the electrode surfaces $S_e \subset S$ and would like to model the injected current I . There are different types of electrodes and resulting equations.[53] For the reciprocity approach we may use two voltage electrodes with constant applied voltage $\pm V_e$. Carefully note that this is not the voltage measured at the electrodes due to a cortical source but the stimulation voltage in the independent problem of determining the electric field E due to electrode stimulation. We can use Coulomb's law to determine the voltage at the electrode e_k and again solve for $\frac{\rho}{\varepsilon_0}$. At the stimulation electrodes we obtain the following equation (see [53]).

Definition 4.1.4 (BEM-FMM integral equation at electrodes). *For all $r \in S_{e_k}$ we have*

$$\int_S \frac{1}{4\pi} \frac{\rho(r')}{|r - r'|} dr' = V_k. \quad (4.14)$$

V_k is the voltage applied at electrode e_k , $k = 1, 2$ and is either V_e or $-V_e$.

In summary, we have two types of equations on S when using the Helmholtz reciprocity approach: One on the conductivity boundaries S_c and another at the electrodes S_e .

Once we solve this problem for ρ , we have determined the charge distribution resulting from electrode stimulation with constant voltage V_e . In order to now apply the reciprocity principle (Equation 4.12), we need to determine the current I_k which is introduced at electrode e_k . As stated in [53], we can do so with the following formula for I .

Definition 4.1.5 (BEM-FMM electrode current). *The induced current I at an electrode S_{e_k} can be determined from the electric field E in the direction of the inner normal $-n(r)$ and the*

conductivity inside the tissue the electrode is located at $\sigma_{in}(r)$ by the following equation

$$I_k = \int_{S_{e_k}} - \langle \sigma_{in} E_{in}(r), n(r) \rangle dr. \quad (4.15)$$

Here, E_{in} is the same limit as in Equation 4.5 but without the primary field

$$E_{in}(r) = \int_S \frac{1}{4\pi} \frac{\rho(r')(r-r')}{|r-r'|^3} dr' - \frac{1}{2} \rho(r)n(r). \quad (4.16)$$

In conclusion, we have to solve the combination of Definition 4.1.3 and 4.1.4 for ρ . We then derive the induced current via Definition 4.1.5 and can use Helmholtz reciprocity (Equation 4.12) to apply the results to different forward problems.

4.2 A Galerkin Approach

In order to be able to deal with the above problems computationally, with primary field or with electrode stimulation and Helmholtz reciprocity, we need to numerically approximate a solution not unlike we did with the finite element method in chapter 3.3. This procedure has been described in all publications about BEM-FMM or their supplements.[53, 55, 54, 56] Mathematical background is given in standard textbooks about linear integral equations called Fredholm equations, see for example [63].

We represent the surface S as the union of non-overlapping triangles. Let τ be the set of these triangles. We then approximate in the finite dimensional space of the functions that are constant on each triangle.

$$V_\tau = \{v|v|_T \in P^0(T) \text{ for all } T \in \tau\}. \quad (4.17)$$

If $\tau = \{T_1, \dots, T_{n+m}\}$, the so-called ‘‘pulse basis’’ of this space is simply given by the indicator functions $1_{T_1}, \dots, 1_{T_{n+m}}$. Here, T_1, \dots, T_n denote all triangles belonging to the conductivity boundaries and T_{n+1}, \dots, T_m make up the electrode surface S_e if the reciprocity approach is applied. In light of the theory given in [63], we may look at the inner product

$$\langle f, g \rangle_S = \int_S fg dx \quad (4.18)$$

and apply a Galerkin method using an expansion into pulse basis functions.

4.2.1 Modeling the Source Directly

First, we apply this approach to the integral equation given in Definition 4.1.1. We thus would like to solve

$$\langle \rho(r) - 2K \langle \int_S \frac{1}{4\pi} \frac{\rho(r')(r-r')}{|r-r'|^3} dr', n(r) \rangle, g \rangle_S = \langle 2K \langle E^p(r), n(r) \rangle, g \rangle_S. \quad (4.19)$$

for all $g \in V_\tau$. We expand $\rho(r)$ into pulse basis functions $\rho(r) = \sum_{i=1}^n c_i 1_{T_i}(r)$. The above is equivalent to solving

$$\begin{aligned} \int_S \sum_{i=1}^n c_i 1_{T_i}(r) 1_{T_j}(r) dr - \int_S 2K < \int_S \frac{1}{4\pi} \frac{\sum_{i=1}^n c_i 1_{T_i}(r')(r-r')}{|r-r'|^3} dr', n(r) > 1_{T_j}(r) dr \\ = \int_S 2K < E^p(r), n(r) > 1_{T_j}(r) dr \end{aligned} \quad (4.20)$$

for all $1 \leq j \leq n$. We can reformulate this as

$$A_j c_j - \sum_{i=1}^n c_i \int_{T_j} 2K < \int_{T_i} \frac{1}{4\pi} \frac{(r-r')}{|r-r'|^3} dr', n_j > dr = \int_{T_j} 2K < E^p(r), n_j > dr, \quad (4.21)$$

where A_j is the area of triangle T_j and n_j is its unit outer normal. Dividing by A_j , we end up with the following system of linear equations.

Lemma 4.2.1. *Let the matrix A be defined as*

$$A_{ji} = \delta_{ij} - \frac{1}{A_j} \int_{T_j} 2K < \int_{T_i} \frac{1}{4\pi} \frac{(r-r')}{|r-r'|^3} dr', n_j > dr. \quad (4.22)$$

Let further b be defined as

$$b_j = \frac{1}{A_j} \int_{T_j} 2K < E^p(r), n_j > dr. \quad (4.23)$$

Then the linear problem

$$Ac = b \quad (4.24)$$

is equivalent to solving the problem given in Definition 4.1.1 in the space V_τ via the identification $c \mapsto \sum_{j=1}^n c_j 1_{T_j}$.

Once a solution is found, applying Coulomb's law to derive the secondary potential resulting from a cortical source is reduced to the computation of

$$\varphi^s(r) = \sum_{i=1}^n c_i \int_{T_i} \frac{1}{4\pi} \frac{1}{|r-r'|} dr'. \quad (4.25)$$

4.2.2 Helmholtz Reciprocity

The integral equation without primary field (Definition 4.1.3) only differs in the right-hand side. The formulation is thus very similar to the above. The integral equation at the electrodes (Definition 4.1.4) in our Galerkin approach can be written as

$$\int_S \int_S \frac{1}{4\pi} \frac{\sum_{i=1}^n c_i 1_{T_i}(r)}{|r-r'|^3} dr' 1_{T_j}(r) dr = \int_S V_e 1_{T_j}(r) dr \quad (4.26)$$

for all T_j belonging to the electrode surface S_e . This is equivalent to

$$\sum_{i=1}^n c_i \int_{T_j} \int_{T_i} \frac{1}{4\pi} \frac{1}{|r-r'|^3} dr' dr = A_j V_e. \quad (4.27)$$

We may divide by A_j and end up with the following linear system of equations.

Lemma 4.2.2. *Let the matrix A be defined as*

$$A_{ji} = \delta_{ij} - \frac{1}{A_j} \int_{T_j} 2K \langle \int_{T_i} \frac{1}{4\pi} \frac{(r-r')}{|r-r'|^3} dr', n_j \rangle dr \quad (4.28)$$

for $1 \leq j \leq n$ and as

$$A_{ji} = \frac{1}{A_j} \int_{T_j} \int_{T_i} \frac{1}{4\pi} \frac{1}{|r-r'|} dr' dr \quad (4.29)$$

for $n < j \leq n+m$. Let further b be defined as $b_j = 0$ for $1 \leq j \leq n$ and as $b_j = V_k$ for $n < j \leq n+m$ and $T_j \subset S_{e_k}$. Then the linear problem

$$Ac = b \quad (4.30)$$

is equivalent to solving the problem given in Definition 4.1.3 and 4.1.4 in the space V_τ via the identification $c \mapsto \sum_{j=1}^n c_j 1_{T_j}$.

Once solved, we derive the induced current at the electrode like in Definition 4.1.5 given by

$$I_k = - \sum_{T_j \subset S_{e_k}} \left(\int_{T_j} \langle \sigma_{\text{in}} \sum_{i=1}^n c_i \int_{T_i} \frac{1}{4\pi} \frac{(r-r')}{|r-r'|^3} dr', n_j \rangle dr - \frac{1}{2} \sigma_{\text{in}} A_j c_j \right). \quad (4.31)$$

We then use Helmholtz reciprocity and find forward solutions by using

$$V = -\frac{1}{I} \langle \sum_{i=1}^n c_i \int_{T_i} \frac{1}{4\pi} \frac{(x_0-r')}{|x_0-r'|^3} dr', M \rangle. \quad (4.32)$$

4.3 Computational Details

4.3.1 Use of the Fast Multipole Method

In all of the above equations needed for both approaches, we are tasked with computing Coulombic interaction and need to determine both electric field and potential integrals. We may use center-point approximations. For the approach with an explicit model of the source, this leads to approximations of the integrals in Equations 4.22, 4.23 and 4.25. First, we have

$$\begin{aligned} (Ac)_j &= \sum_{i=1}^n \left(\delta_{ij} - \frac{1}{A_j} \int_{T_j} 2K \langle \int_{T_i} \frac{1}{4\pi} \frac{(r-r')}{|r-r'|^3} dr', n_j \rangle dr \right) c_i \\ &= c_j - \sum_{i=1}^n \frac{1}{A_j} \int_{T_j} 2K \langle \int_{T_i} \frac{1}{4\pi} \frac{c_i(r-r')}{|r-r'|^3} dr', n_j \rangle dr \\ &\approx c_j - 2K \langle \sum_{\substack{i=1 \\ i \neq j}}^n \frac{(A_i c_i)(r_j - r_i)}{|r_j - r_i|^3}, n_j \rangle, \end{aligned} \quad (4.33)$$

where r_i is the center of triangle T_i . Next, the right-hand side is

$$b_j = \frac{1}{A_j} \int_{T_j} 2K \langle E^p(r), n_j \rangle dr \approx 2K \langle E^p(r_j), n_j \rangle. \quad (4.34)$$

The secondary potential is approximated as

$$\varphi^s(r) = \sum_{i=1}^n \left(\int_{T_i} \frac{1}{4\pi} \frac{1}{|r-r'|} dr' \right) c_i \approx \frac{1}{4\pi} \sum_{i=1}^n \frac{(A_i c_i)}{|r-r_i|}. \quad (4.35)$$

Most of the computational effort goes into computing the terms

$$\begin{aligned} & \sum_{i=1}^n \frac{(A_i c_i)}{|r-r_i|} \\ & \sum_{\substack{i=1 \\ i \neq j}}^n \frac{(A_i c_i)(r_j - r_i)}{|r_j - r_i|^3}. \end{aligned} \quad (4.36)$$

This is a natural application of the three-dimensional fast multipole method (FMM, see chapter 5). The algorithm approximates particle interaction between a set of sources and targets in an efficient manner up to a user-specified precision. In the above equation the strengths of the sources r_1, \dots, r_n are given by $A_i c_i$. We assume the charge on triangle T_i to be constant. The total charge of the triangle is thus $A_i c_i$ and it is then assigned to r_i in our center-point approximation. Using the FMM, the core computational effort can be greatly reduced. Instead of actually setting up and storing the matrix A , the FMM allows us to execute the matrix-vector product Ac in a matrix-free fashion. This coupling with the FMM is what makes the BEM-FMM approach computationally feasible in the first place. It can also be used (see Definition 4.1.2) for the computation of the primary field E^p , needed for the right-hand side b , and the primary potential φ^p which together with the secondary potential φ^s yields the solution of a forward problem.

We may also use center-point approximation for the reciprocity approach. The rows $1 \leq j \leq n$ of the matrix A are the same, only rows $n < j \leq n+m$ corresponding to electrode triangles change. For Equation 4.29, we have

$$(Ac)_j \approx \frac{1}{4\pi} \sum_{\substack{i=1 \\ i \neq j}}^n \frac{(A_i c_i)}{|r_j - r_i|}. \quad (4.37)$$

Next, the induced current (Equation 4.31) is approximated using

$$I_k \approx - \sum_{T_j \subseteq S_{e_k}} A_j \sigma_{\text{in}} \left(\left\langle \frac{1}{4\pi} \sum_{\substack{i=1 \\ i \neq j}}^n \frac{(A_i c_i)(r_j - r_i)}{|r_j - r_i|^3}, n_j \right\rangle - \frac{1}{2} c_j \right). \quad (4.38)$$

Finally, the voltage difference (Equation 4.32) is

$$V \approx -\frac{1}{I} \left\langle \frac{1}{4\pi} \sum_{i=1}^n \frac{(A_i c_i)(x_0 - r_i)}{|x_0 - r_i|^3}, M \right\rangle. \quad (4.39)$$

We can thus once more make use of the FMM for each of these equations in order to compute the potential or field at a set of targets generated by a set of sources with given source strength.

4.3.2 Interaction between Near Neighbors

Center-point approximations and the resulting use of the FMM fail if two triangles and their centers r_j, r_i are too close. For a preset number of nearest neighbors of a point r_j we thus replace these with more exact terms. This process has been presented in [56].

In the direct approach we make use of a Gaussian quadrature rule for the primary field if the triangle T_j and the center of the dipole $\frac{x_0+x'_0}{2}$ are too close. This general quadrature rule is given as convex coefficients $\lambda_{1p}, \lambda_{2p}, \lambda_{3p}$ for $p = 1, \dots, k$ and corresponding weights w_p . We then approximate the primary field in the context of the right-hand side b (Equation 4.23) by

$$b_j = \frac{1}{A_j} \int_{T_j} 2K \langle E^p(r), n_j \rangle dr \approx \frac{1}{A_j} A_j \sum_{p=1}^k w_p 2K \langle E^p(r_j^p), n_j \rangle dr, \quad (4.40)$$

where r_j^p is the convex combination $\lambda_{1p}x_j^1 + \lambda_{2p}x_j^2 + \lambda_{3p}x_j^3$ of the three vertices of triangle T_j . Note that we multiply by the area A_j as the quadrature rule is normalized to 1. If an evaluation point r_j and the dipole center are too close, we can do the same for the primary potential (Equation 4.10) which is needed to compute the full potential at r_j

$$\varphi^p(r_j) = \frac{I_0}{4\pi\sigma|r_j - x_0|} - \frac{I_0}{4\pi\sigma|r_j - x'_0|} \approx \sum_{m=1}^k w_m \left(\frac{I_0}{4\pi\sigma|r_j^m - x_0|} - \frac{I_0}{4\pi\sigma|r_j^m - x'_0|} \right). \quad (4.41)$$

A similar approach is used in the context of the potential generated by all surface charges. This is needed when computing the secondary field $\varphi^s(r_j)$ at a point r_j in the direct approach (Equation 4.25)

$$\varphi^s(r_j) = \sum_{i=1}^n \left(\int_{T_i} \frac{1}{4\pi} \frac{1}{|r_j - r'|} dr' \right) c_i. \quad (4.42)$$

Now if the target r_j and one of the source triangles T_i are too close, center-point approximation and FMM will not work.

Definition 4.3.1. *We assign to each source point r_i a set of l nearest neighbors NN_h . We then define the matrix PC as*

$$PC_{ji} = -\frac{1}{4\pi} \frac{A_i}{|r_j - r_i|} + \sum_{m=1}^k w_m \int_{T_i} \frac{1}{4\pi} \frac{1}{|r_j^m - r_i|} dr', \quad (4.43)$$

if $j \in NN_i$ and $PC_{ji} = 0$ otherwise.

Now, we can proceed as follows. First, we use center-point approximations for all interactions of sources r_i with the particle r_j . We thus compute the full FMM contribution for all sources and then simply add $(PCc)_j$. This term first subtracts the contribution of the FMM for a few near sources and then adds a more precise computation of the contribution of T_i to the potential at T_j . The integral in the above definition can be calculated analytically using the formula described in [64]. These terms PC_{ji} are precalculated for a certain number of near neighbors of each source point r_i . Later, the resulting matrix PC only has to be multiplied with c and added to the

result of the FMM in order to correct the inaccuracies of center-point approximations for near neighbors.

The linear equations at the electrode triangles in the reciprocity approach (Equation 4.29) involve a similar term and we can use *PC* there as well. If we only use center-point approximation for the outer integral over T_j but not for the inner integral, we have

$$(Ac)_j = \sum_{i=1}^n \left(\frac{1}{A_j} \int_{T_j} \int_{T_i} \frac{1}{4\pi} \frac{1}{|r-r'|} dr' dr \right) c_i \approx \sum_{i=1}^n \left(\int_{T_i} \frac{1}{4\pi} \frac{1}{|r_j-r'|} dr' \right) c_i \quad (4.44)$$

for $n < j \leq n+m$. Once more, we can first compute the full FMM before adding *PCc* in order to calculate $(Ac)_j$ more precisely.

We can follow a similar approach for the normal electric field

$$\frac{1}{A_j} \int_{T_j} < \int_{T_i} \frac{1}{4\pi} \frac{(r-r')}{|r-r'|^3} dr', n_j > dr. \quad (4.45)$$

This term is of interest for the matrix vector product Ac for both the direct (Equation 4.22) and the reciprocity (Equation 4.28) approach. It is also needed for the computation of the current (Equation 4.31). We see that

$$\frac{1}{A_j} \int_{T_j} < \int_{T_i} \frac{1}{4\pi} \frac{(r-r')}{|r-r'|^3} dr', n_j > dr = \frac{1}{A_j} \frac{1}{4\pi} \int_{T_i} < \int_{T_j} \frac{(r-r')}{|r-r'|^3} dr, n_j > dr'. \quad (4.46)$$

We use our Gaussian quadrature for the outer integral and can define the matrix EC .

Definition 4.3.2. We assign to each source point r_i another set of l' nearest neighbors NN'_h . We define the matrix EC as

$$EC_{ji} = - < \frac{1}{4\pi} \frac{(A_i c_i)(r_j - r_i)}{|r_j - r_i|^3}, n_j > + \frac{1}{A_j} \frac{1}{4\pi} A_i \sum_{m=1}^k w_m < \int_{T_j} \frac{(r - r_i^m)}{|r - r_i^m|^3} dr, n_j > \quad (4.47)$$

if $j \in NN'_i$ and $EC_{ji} = 0$, otherwise.

The inner integral term in normal direction

$$< \int_{T_j} \frac{(r - r_i^m)}{|r - r_i^m|^3} dr, n_j > \quad (4.48)$$

can be computed analytically using [65]. We can now proceed as we did with *PC*. First, we compute the normal electric field using the FMM. Then we add the matrix-vector product ECc which subtracts the FMM results for a few near sources and adds more precise computations instead. The computation of *PC* and *EC* is parallelized using the MATLAB[66] native “parfor” loop.

4.3.3 Conservation Laws, Preconditioners and Mesh Refinement

In the direct approach, the global charge conservation law must be upheld. It states that

$$\int_S \rho(r) dr = 0. \quad (4.49)$$

This is not explicitly implemented in our integral equation. Instead, [55] reports that a normalized version

$$\frac{1}{|S|} \int_S \rho(r) dr = 0 \quad (4.50)$$

is added to the main equation in the following form. Let w be a weighting scalar (usually set to 0.5), then instead of solving $Ac = b$ we solve

$$Ac + w \frac{1}{\sum_{i=1}^n A_i} \sum_{i=1}^n A_i c_i = b. \quad (4.51)$$

In the case of the reciprocity approach we would like to enforce the global Kirchhoff's current conservation law as is stated in [53]. We have derived a way to compute the total current of an electrode in Definition 4.1.5 and Equations 4.31 and 4.38 with correction by using *PC*. These ideas can also be used for the following. Instead of solving $Ac = b$, we solve

$$Ac + w \frac{1}{\sum_{i=n+1}^{n+m} \sigma_{in_i} A_i} \sum_{k=1}^2 -I_k = b. \quad (4.52)$$

For the reciprocity approach, a preconditioner matrix is applied to the m equations formulated at the electrodes (Equation 4.29).[53] This $m \times m$ matrix is simply defined as the matrix

$$M_{ji} = \frac{1}{A_j} \int_{T_j} \int_{T_i} \frac{1}{4\pi} \frac{1}{|r - r'|} dr' dr. \quad (4.53)$$

This is exactly the matrix which would result if we would only have electrode surfaces. M is computed using center-point approximation and more precise terms for near neighbors.

Finally, when the triangles belonging to electrodes are chosen, these are refined by adding nodes at the centers of the three edges and connecting them to each other with new edges. One triangle is thus refined into 4 triangles. The mesh is also refined in the same manner if tissue boundaries are too close to each other.

All of this has been implemented in MATLAB[66], except for the FMM (see chapter 5), and the MATLAB native generalized minimum residual method is used to solve the linear system. Exemplary code for the direct approach can be found at a GitHub repository[67] and for the reciprocity approach at a Dropbox folder[68].

Chapter 5

The Fast Multipole Method

We are interested in the pairwise interaction of a large set of particles. Namely, we would like to evaluate

$$\Phi(r_i) = \sum_{\substack{j=1 \\ j \neq i}}^N q_j \frac{1}{|r_i - r_j|} \quad (5.1)$$

and in our case especially its gradient field for all $i = 1, \dots, N$. This is an application in the context of electrostatics, but particle interaction is a common problem in computational physics. The above can also be seen in the context of gravitation with q_j being the (always positive) mass of a body located at r_j . There exist further, similar N -body problems with other interaction kernels than this one. They all share a common obstacle.

If one follows the notation of Equation 5.1 and uses the canonical method of computing the interaction exactly like it is written down, the effort is of the order $O(N^2)$ (see any standard textbook for details on the big O Landau notation). The fast multipole method (FMM) provides an efficient way to approximate these interactions up to a requested precision and is used excessively in many different fields. It is based on a far field approximation and hierarchical decomposition of the domain. The FMM was first introduced by Leslie Greengard and Vladimir Rokhlin Jr. in 1987[69] and has been named as one of the top ten algorithms of the 20th century alongside methods like Krylov subspace approximations or Quicksort by SIAM editors[70]. There exists a variety of lectures and literature on the method and further improvements have been made until this day (e.g. [71]). The following chapter is oriented after [72, 73, 69].

We start this chapter by motivating and deriving the conceptual idea behind the fast multipole method with the aid of a simplified, exemplary far field approximation without mathematical background or error bounds. The second part then deals with the analytical machinery necessary for a more precise approximation using multipole expansion and actual error bounds. We modify the algorithm according to these details and arrive at the FMM. We conclude with a few notes about computational bottlenecks and improvements made on the original method presented here.

5.1 The Concept

Our goal is to evaluate a function of the form

$$\Phi(y_i) = \sum_{j=1}^N q_j K(r_j, y_i) \quad (5.2)$$

with K being an interaction kernel. Oftentimes, sources r_i and targets y_j equal as is the case with BEM-FMM. In the following, we assume sources and targets to be equal but only minor, obvious modifications are necessary for (partially) different sets.

A key idea behind the fast multipole method is far field expansion. The kernel $K(r_j, r_i)$ can be written as a series if there is a certain distance between sources r_j and targets r_i . By only using a number of expansion terms it can then be approximated by a finite sum of the form $\sum_{k=1}^p f_k(r_j)g_k(r_i)$ with error bounds depending on the number of terms p . As the terms for sources and targets are now split, the terms for clusters of sources can be grouped together and their influence on distant targets calculated as one. Of course, this only holds for far fields and we will need to think of a clever way to determine these clusters and their pairwise influence on another.

Before diving into mathematical details, analytic considerations and error bounds for the FMM, we would like to motivate and derive the algorithmic concept behind it in a simplified setting. For this, we will use an unprecise far field approximation which consists of only one term.



Figure 5.1: The far field interaction of all sources contained in box B with all targets in a sufficiently distant box A.

Let us start with the setting depicted in Figure 5.1. Please note that the figures in this chapter are two dimensional and we are mainly interested in a three dimensional FMM in the context of BEM-FMM. A and B are two boxes sufficiently distant so that we can use our approximation. Box B contains a set of sources and we would like to determine their interaction with all targets contained in box A, i.e.

$$\sum_{r_j \in B} q_j K(r_j, r_i) \quad (5.3)$$

for all $r_i \in A$. The simplified far field approximation from the viewpoint of A now consists in representing the cluster of all sources $r_j \in B$ with loads q_j as one total charge $q_B = \sum_{r_j \in B} q_j$ located at the center r_B of B. Furthermore, we evaluate the far field at the center r_A and not at the target locations $r_j \in A$. We thus approximate Equation 5.3 by

$$q_B K(r_B, r_A). \quad (5.4)$$

This approximation reduces the number of operations for the interaction from B to A from $O(N_B N_A)$ to $O(N_B + N_A)$, where N_B, N_A denote the number of particles in B and A, respectively. First, we compute q_B and then we assign the far field approximation to each $r_j \in A$. How can we translate this idea to a set of particles, which are neither guaranteed to have a sufficient distance nor can we distinguish between sources and targets as all particles serve as both to one another?

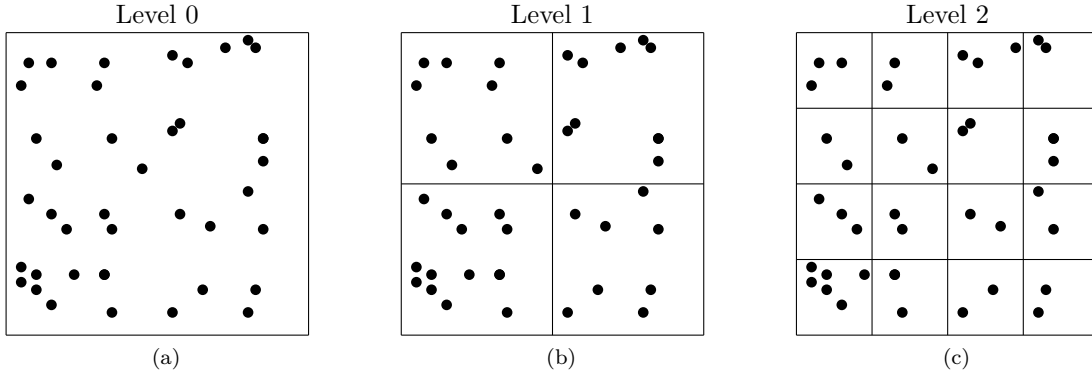


Figure 5.2: The domain is hierarchically partitioned into boxes of decreasing size. (a) The level 0 box contains all particles. (b) and (c) All boxes are divided into subboxes with each refinement step.

The central idea is to cluster particles at different levels of refinement by using a hierarchical decomposition of the domain as illustrated in Figure 5.2. Interactions between clusters with sufficient distance can then be computed as described above and only interactions between near particles need to be handled directly. With each refinement step of the boxes, a greater part of the interaction can be calculated by using far field approximation.

At refinement level 0 we only have one box which contains all particles (Figure 5.2a). Refinement level $l + 1$ is obtained from level l by dividing each box into 8 equal parts (4 parts in two dimensions). This process yields refinement levels 1 and 2 as illustrated in Figure 5.2b and Figure 5.2c.

At level 0 we only have one box. At level 1 all boxes are close to one another and we make the following definition.

Definition 5.1.1 (Near neighbor). *If two boxes are at the same refinement level and share a boundary point, we call them near neighbors. A box is a near neighbor to itself.*

The interaction between near neighbors can not be approximated using the far field. We thus refine all boxes again and now have boxes which are not near neighbors.

Definition 5.1.2 (well separated). *If two boxes are at the same refinement level and are not near neighbors we call them well separated.*

The particles contained in two well separated boxes have a distance of at least the edge length of the box and we make use of the far field approximation. First, we compute the total charge q_B

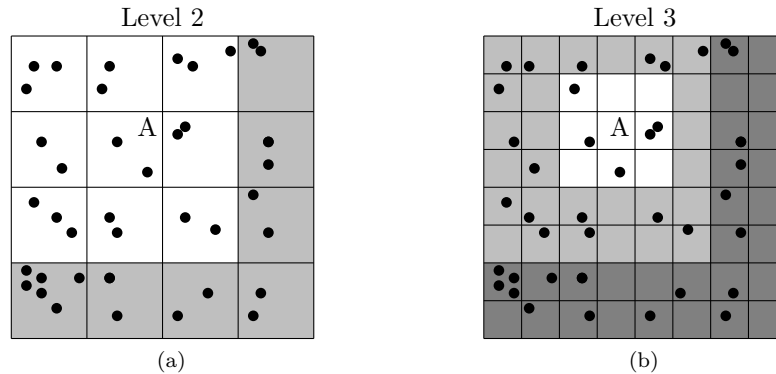


Figure 5.3: (a) Near neighbors of A are white, while well separated boxes are marked light gray. (b) Near neighbors of A are white, the interaction list is marked light gray and the dark gray boxes have been considered at the previous refinement level.

for every box B at refinement level 2. Given a particle in a box A at level 2, we can now sum the far fields $q_B K(r_B, r_A)$ for all B that are well separated from A. Figure 5.3a illustrates this. We now have taken care of the interaction with all particles in boxes marked light gray. This can be done for every box A at level 2. How do we proceed with the remaining interactions?

Of course, we refine into subboxes again. Once more, we calculate q_B for every box B at refinement level 3. Looking at a particle in a level 3 box A, some of the other particles are contained in near neighbors, some have been taken care of at level 2, but there remains a set of boxes which are now newly well separated.

Definition 5.1.3 (interaction list). *The interaction list of a box A is the set of subboxes of near neighbors of A's parent which are well separated from A.*

An interaction list is illustrated in Figure 5.3b and contains exactly the boxes with new far fields we can now add. They are well separated and have not yet been taken into account as they were too close in previous levels. For each particle in a box A at level 3 we thus add the far fields $q_B K(r_B, r_A)$ of all B in the interaction list of A. We now have taken care of all interactions by third-level well separated boxes B for all particles.

This can be repeated for each refinement step, and by iterating over all levels from coarse to fine partitions, we have found a way to compute most of the interactions by means of far field approximations. At the end, we will have to add the exact interaction with the remaining particles. The resulting algorithm is stated in Algorithm 1.

Algorithm 1 The $O(N \log N)$ algorithm

```

// Compute the total load for every box
for  $l = 2, \dots, l_{\max}$  do
  for boxes B on refinement level  $l$  do
     $q_B \leftarrow \sum_{r_j \in B} q_j$ 
  end for
end for

// Consider all far field interactions
for  $l = 2, \dots, l_{\max}$  do
  for boxes A on refinement level  $l$  do
    for boxes B in interaction list of A do
      for particles  $r_i$  in A do
         $\Phi(r_i) \leftarrow \Phi(r_i) + q_B K(r_B, r_A)$ 
      end for
    end for
  end for
end for

// Add exact interaction with near particles
for boxes A on refinement level  $l_{\max}$  do
  for particles  $r_i$  in A do
    for particles  $r_j$  in near neighbors of A do
       $\Phi(r_i) \leftarrow \Phi_A + q_j K(r_j, r_i)$ 
    end for
  end for
end for

```

Let us analyse the computational difficulty of this algorithm. First, we have $O(Nl_{\max})$ operations for computing all total loads. Each particle is contained in exactly one box and thus each of the N particles is considered once at each of the $l_{\max} - 1$ refinement levels. For the far field interactions, we note that there is a constant number bounding the size of all interaction lists (189 in three dimensions). At each refinement level, we look at each particle and compute the far field interaction with all boxes in the interaction list. This code block thus runs at a cost of $O(Nl_{\max})$. As a last step, the interaction with the remaining, near particles needs to be assessed. In three dimensions, a partition of a box yields 8 subboxes. Thus, at level n we have 8^n boxes. Assuming for now a fairly homogeneous distribution of points, we may use $l_{\max} = \log_8 N$ refinement levels and see that we end up with N leaf-boxes (a box without subboxes). At the last level, each box only contains $O(1)$ particles. As the number of near neighbors is bounded by 27, the last step runs in $O(N)$. In conclusion, Algorithm 1 is of complexity $O(N \log N)$.

This can be further improved. We observe that if B_1, \dots, B_8 are the subboxes of B then $q_B = q_{B_1} + \dots + q_{B_8}$. We can derive the total load of B with 8 operations from the loads of its subboxes. Our new approach consists of starting with q_B for all the leaf-boxes. Then we iterate over all levels from finest to coarsest and derive q_B from its subboxes which were computed in the previous step. At the finest level, we have an effort of $O(N)$ as each particle is considered once. At a coarser level l , we have 8^l boxes each with 8 subboxes. Now

$$O\left(\sum_{l=2}^{\log_8 N-1} 8^{l+1}\right) = O(N). \quad (5.5)$$

We turn to the far field interactions. As they are constant per box A , we could assign them to the target boxes on each refinement level instead of the particles. We have 8^l boxes per level l with bounded interaction lists plus one parent box and as we just saw this results in a complexity of $O(N)$. Let us summarize this modified algorithm.

Algorithm 2 The $O(N)$ algorithm

```

// Compute the total load for every leaf-box
for boxes  $B$  on refinement level  $l_{\max}$  do
     $q_B \leftarrow \sum_{r_j \in B} q_j$ 
end for

// Compute the total load for every box
for  $l = l_{\max}, \dots, 2$  do
    for boxes  $B$  on refinement level  $l$  do
         $q_B \leftarrow \sum_{\text{subboxes } B' \text{ of } B} q_{B'}$ 
    end for
end for

// Consider all far field interactions per box
for  $l = 2, \dots, l_{\max}$  do
    for boxes  $A$  on refinement level  $l$  do
         $\Phi_A \leftarrow \Phi_{\text{parent of } A}$ 
        for boxes  $B$  in interaction list of  $A$  do
             $\Phi_A \leftarrow \Phi_A + q_B K(r_B, r_A)$ 
        end for
    end for
end for

// Assign far field and near interaction to actual particles
for boxes  $A$  on refinement level  $l_{\max}$  do
    for particles  $r_i$  in  $A$  do
        for particles  $r_j$  in near neighbors of  $A$  do
             $\Phi(r_i) \leftarrow \Phi_A + q_j K(r_j, r_i)$ 
        end for
    end for
end for

```

Finally, we have derived an algorithm with a computational effort of $O(N)$. Of course our approximation by the center point and the sum of loads is not precise. It only served as a simplification in order to make the algorithm itself and the motivation behind it easier to understand and allowed us to leave out difficult and long mathematical specifics. We will use a different approximation in the mathematical derivation following in the next chapter allowing us to derive error bounds and arbitrary precision. We will also need to modify Algorithm 2 at a few points due to the more complicated nature of the far field approximation but the key ideas remain the same.

Usually, the distribution of particles is not homogeneous as is the case in our application. We can modify the refinement tree in such a way that only those boxes are divided that contain a large number of particles. Resulting empty boxes are forgotten. The description is more involved as for example non-refined boxes need to be considered as near interaction even though they are on another refinement level, but the computational efficiency is retained.[74] Actually, there exist methods in competition of FMM concerning runtime in homogeneous settings, but the fast multipole method has few competitors for non-uniform distributions.

5.2 Mathematical Details

We are interested in a far field approximation of the electric potential. Given two particles, the interaction kernel is

$$K(r_j, r_i) = \frac{1}{|r_i - r_j|}. \quad (5.6)$$

We would like to derive a series expansion of this kernel. Let us write the particle locations r_i in spherical coordinates $(\lambda_i, \alpha_i, \beta_i)$. Now

$$|r_i - r_j|^2 = \langle r_i, r_i \rangle + \langle r_j, r_j \rangle - 2 \langle r_i, r_j \rangle = \lambda_i^2 \left(1 + \frac{\lambda_j^2}{\lambda_i^2} - 2 \frac{\lambda_j}{\lambda_i} \frac{\langle r_i, r_j \rangle}{\lambda_i \lambda_j} \right). \quad (5.7)$$

We define $x = \frac{\lambda_j}{\lambda_i}$ and $y = \frac{\langle r_i, r_j \rangle}{\lambda_i \lambda_j}$ and are now faced with the term

$$\frac{1}{\lambda_i \sqrt{(1 + x^2 - 2xy)}}. \quad (5.8)$$

The theory of the Legendre Polynomials P_n , $n = 0, 1, \dots$, provides us with the means of expanding this into a power series of x . [75] For $|x| < 1$, i.e. for targets r_i further away from zero than all sources r_j , we have

$$K(r_j, r_i) = \frac{1}{\lambda_i} \sum_{n=0}^{\infty} P_n(y) x^n = \sum_{n=0}^{\infty} P_n(y) \frac{\lambda_j^n}{\lambda_i^{n+1}}. \quad (5.9)$$

The condition $|r_j| = \lambda_j < \lambda_i = |r_i|$ needed for this series expansion reflects our aspiration of finding a far field representation but unfortunately this expansion does not meet our needs. The term y depends on both sources and targets. The theory of the Laplace equation, also known as the potential equation, deals with spherical harmonics Y_n^m , $n = 0, 1, \dots$ and $m = -n, \dots, n$. For further details see any standard textbook, for example [75], and of course the original work on the fast multipole method [73]. Important for us is that spherical harmonics enable us to split sources from targets using the addition theorem for Legendre Polynomials. It states that for r_i, r_j in spherical coordinates as above, we have

$$P_n(y) = P_n\left(\frac{\langle r_i, r_j \rangle}{\lambda_i \lambda_j}\right) = \sum_{m=-n}^n Y_n^{-m}(\alpha_j, \beta_j) Y_n^m(\alpha_i, \beta_i). \quad (5.10)$$

We can plug this into Equation 5.9 and end up with the desired expansion. For now we have looked at a source r_j centered at zero and a target r_t with $|r_t - 0| > |r_j - 0|$. For the fast multipole method we are interested in a far field expansion at the center r_B of a box of sources. The following theorem summarizes our efforts and provides error bounds for approximations. The series we have derived is called multipole expansion. In the following we will only state the necessary mathematical tools needed for the FMM and proves of the theorems can be found for example in [73].

Theorem 5.2.1 (Multipole expansion). *Let charges q_1, \dots, q_k be located at r_1, \dots, r_k with $|r_j - r_c| < R$ for a center point r_c . Let $r_j - r_c$ be given by $(\lambda_j, \alpha_j, \beta_j)$ in spherical coordinates. Given any target point of interaction r_t with $|r_t - r_c| > R$ and $r_t - r_c$ given by $(\lambda_t, \alpha_t, \beta_t)$ in spherical coordinates, we have*

$$\Phi(r_t) = \sum_{j=1}^k q_j \frac{1}{|r_t - r_j|} = \sum_{n=0}^{\infty} \sum_{m=-n}^n M_n^m Y_n^m(\alpha_t, \beta_t) \frac{1}{\lambda_t^{n+1}} \quad (5.11)$$

with

$$M_n^m = \sum_{j=1}^k q_j Y_n^{-m}(\alpha_j, \beta_j) \lambda_j^n. \quad (5.12)$$

If we approximate the series using $p \geq 1$ terms, we have an error bound of

$$|\Phi(r_t) - \sum_{n=0}^p \sum_{m=-n}^n M_n^m Y_n^m(\alpha_t, \beta_t) \frac{1}{\lambda_t^{n+1}}| \leq \frac{\sum_{j=1}^k |q_j|}{\lambda_t - R} \left(\frac{R}{\lambda_t} \right)^{p+1}. \quad (5.13)$$

We note that multipole expansion is only valid outside a ball $B_R(r_c)$ containing all sources r_1, \dots, r_k . We have control over the approximation error via Equation 5.13. Important parameters are the relative distance of sources and targets, expressed in the factor $\frac{R}{\lambda_t}$ and the number of terms p . In chapter 5.1, we used far field approximation for all boxes well separated. If d is the edge length of a box B at a certain refinement level, then a ball of radius $\frac{\sqrt{3}d}{2}$ around r_B is needed to enclose the box. In this setting, the distance factor $\frac{R}{\lambda_t}$ between sources and targets is bounded by $\frac{\sqrt{3}}{3}$ as $\frac{3d}{2}$ is the shortest distance possible between r_B and a target. Now if a certain precision of our computation ε is required, we can choose $p = \lceil -\log_{\sqrt{3}} \varepsilon \rceil$ and thus guarantee an error bound

$$\left(\frac{R}{\lambda_t} \right)^{p+1} \leq \frac{\sqrt{3}^p}{3} = \varepsilon. \quad (5.14)$$

In analogy to Algorithm 1 this is all that is needed for an $O(N \log N)$ algorithm. We summarize in Algorithm 3.

We note that the computational effort of addition of the loads has now risen to operations for $n = 0, \dots, p$ and $m = -n, \dots, n$. This is also the case in the second code block which follows the approximation from Equation 5.13. We see that the overall complexity of the algorithm is given by $O(p^2 N \log N)$.

Algorithm 3 The $O(N \log N)$ multipole algorithm

```

// Compute the multipole expansion for every box
for  $l = 2, \dots, l_{\max}$  do
  for boxes B on refinement level  $l$  do
    Compute  $M_n^m$  for  $n = 0, \dots, p$  and  $m = -n, \dots, n$  centered at  $c_B$  for all particles
    contained in B after Equation 5.12 .
  end for
end for

// Consider all far field interactions
for  $l = 2, \dots, l_{\max}$  do
  for boxes A on refinement level  $l$  do
    for boxes B in interaction list of A do
      for particles  $r_i$  in A do
        Add to  $\Phi(r_i)$  the  $p$ -term multipole approximation of B centered at  $c_B$ 
        like in Equation 5.13.
      end for
    end for
  end for
end for

// Add exact interaction with near particles
for boxes A on refinement level  $l_{\max}$  do
  for particles  $r_i$  in A do
    for particles  $r_j$  in near neighbors of A do
       $\Phi(r_i) \leftarrow \Phi(r_i) + q_j \frac{1}{|r_i - r_j|}$ 
    end for
  end for
end for

```

We would like to improve this as we have done with Algorithm 2, but need additional analytical machinery. We started by computing representations of the far field from the leaf-boxes. Then we only need to accumulate the representations of the subboxes at level $l + 1$ in order to obtain a representation at level l . Given the multipole terms M_n^m for a box at level $l + 1$, we first need to shift the multipole representation to the center of the parent box at level l before we can add them all together.

Theorem 5.2.2 (Translation of a multipole expansion). *Let charges q_1, \dots, q_k be located at r_1, \dots, r_k with $|r_j - r_c| < R$ for a center point r_c . Let further the interaction with any target point r_t outside the source ball, i.e. $|r_t - r_c| > R$ with $r_t - r_c = (\lambda_t, \alpha_t, \beta_t)$, be given by the multipole expansion*

$$\Phi(r_t) = \sum_{n=0}^{\infty} \sum_{m=-n}^n M_n^m Y_n^m(\alpha_t, \beta_t) \frac{1}{\lambda_t^{n+1}} \quad (5.15)$$

as in Theorem 5.2.1. We can translate this into a multipole expansion at r'_c valid outside of $B_{R'}(r'_c)$ with $R' = R + |r_c - r'_c|$. For any point r_t outside of this sphere with $r_t - r'_c = (\lambda'_t, \alpha'_t, \beta'_t)$ we have

$$\Phi(r_t) = \sum_{n=0}^{\infty} \sum_{m=-n}^n K_n^m Y_n^m(\alpha'_t, \beta'_t) \frac{1}{\lambda'_t{}^{n+1}}. \quad (5.16)$$

The new coefficients K_n^m are given by

$$K_n^m = \sum_{j=0}^n \sum_{l=-j}^j \frac{M_{n-j}^{m-l} i^{|m-l|} (-1)^{|m-l|} A_j^l A_{n-j}^{m-l} \lambda_c^j Y_j^{-l}(\alpha_c, \beta_c)}{A_n^m} \quad (5.17)$$

with $r_c - r'_c = (\lambda_c, \alpha_c, \beta_c)$ and

$$A_j^l = \frac{(-1)^j}{\sqrt{(j-l)!(j+l)!}}. \quad (5.18)$$

Finally, we have an error bound for an approximation with $p \geq 1$ of

$$|\Phi(r_t) - \sum_{n=0}^p \sum_{m=-n}^n K_n^m Y_n^m(\alpha'_t, \beta'_t) \frac{1}{\lambda'_t{}^{n+1}}| \leq \frac{\sum_{j=1}^k |q_j|}{\lambda'_t - R'} \left(\frac{R'}{\lambda'_t} \right)^{p+1}. \quad (5.19)$$

We see that it is not necessary to compute the multipole far field approximation centered in r'_c by considering all particles following Theorem 5.2.1. Instead, we can shift the multipole expansion in r_c without a loss in precision (compare Equation 5.19 and Equation 5.13). The process of calculating K_n^m from M_n^m by using Equation 5.17 takes $O(p^4)$ operations. We are now able to compute the multipole terms for each box at all levels representing its far field by translation of the terms M_n^m of all 8 subboxes and addition of the resulting terms K_n^m .

In Algorithm 2, we looked at each box and accumulated all far fields of this target box as a next step. The multipole expansion however is a representation depending on the source box as we use its center as a reference point. Given a target box A and different source boxes B and B' whose far field we would like to assign to A , how do we represent the added far field in a compact manner connected to A ? We need a way to convert a multipole expansion into a local expansion in A .

Theorem 5.2.3 (Conversion of a multipole into a local expansion). *Let charges q_1, \dots, q_k be located at r_1, \dots, r_k inside a sphere $B_R(r_c)$ with a corresponding multipole expansion as in Theorem 5.2.1. If r'_c is the center of a target region and $|r_c - r'_c| > (c + 1)R$ with $c > 1$, then this*

multipole expansion is valid inside the ball $B_R(r'_c)$. We can describe the potential in $B_R(r'_c)$ for $r_t - r'_c = (\lambda_t, \alpha_t, \beta_t)$ using the local expansion

$$\Phi(r_t) = \sum_{n=0}^{\infty} \sum_{m=-n}^n L_n^m Y_n^m(\alpha_t, \beta_t) \lambda_t^n. \quad (5.20)$$

The coefficients L_n^m are given by

$$L_n^m = \sum_{j=0}^n \sum_{l=-j}^j \frac{M_j^l i^{|m-l|-|m|+|l|} A_j^l A_n^m Y_{n+j}^{l-m}(\alpha_c, \beta_c)}{(-1)^j A_{n+j}^{l-m} \lambda_c^{n+j+1}} \quad (5.21)$$

with $r_c - r'_c = (\lambda_c, \alpha_c, \beta_c)$ and A_j^l like in Theorem 5.2.2. Furthermore, we have for any $p \geq 1$

$$|\Phi(r_t) - \sum_{n=0}^p \sum_{m=-n}^n L_n^m Y_n^m(\alpha_t, \beta_t) \lambda_t^n| \leq \frac{\sum_{j=1}^k |q_j|}{cR - R} \left(\frac{1}{c}\right)^{p+1}. \quad (5.22)$$

We can now pick one target box A, compute the coefficients L_n^m for every B in the interaction list of A and add them together. This leads to a compact local representation of the far field created by all particles contained in the interaction list of A. The computational effort is of the order $O(p^4)$ for one pair of source and target box. If d is the edge length of the boxes, a ball of radius $\frac{\sqrt{3}d}{2}$ around their center is needed to cover them. If two boxes are only separated by one shared near neighbor, the distance between their center points can be as small as $2d$ and thus $c < \frac{4}{\sqrt{3}} - 1$. The approximation error thus only decays with a worst case rate of about $\left(\frac{3}{4}\right)^p$ instead of $\left(\frac{\sqrt{3}}{3}\right)^p$ like the multipole expansion.

In order to represent the total far field of a target box A and not only that of its interaction list, we also need to think of the interaction lists of As predecessor (parent, parent's parent, ...). Their far fields were passed on to their subboxes in Algorithm 2. The local expansion from Theorem 5.2.3 and its compact representation as terms L_n^m is valid in subboxes as well but is not expressed in the center of it. We also need to be able to translate the local expansion.

Theorem 5.2.4 (Translation of a local expansion). *Let a local expansion centered in r_c be given by*

$$\Phi(r_t) = \sum_{n=0}^p \sum_{m=-n}^n L_n^m Y_n^m(\alpha_t, \beta_t) \lambda_t^n \quad (5.23)$$

for $r_t - r_c = (\lambda_t, \alpha_t, \beta_t)$. We can shift this representation to the origin r'_c . If $r_t - r'_c = (\lambda'_t, \alpha'_t, \beta'_t)$ then

$$\Phi(r_t) = \sum_{n=0}^p \sum_{m=-n}^n K_n^m Y_n^m(\alpha'_t, \beta'_t) \lambda'_t^n \quad (5.24)$$

with coefficients

$$K_n^m = \sum_{j=n}^p \sum_{l=-j}^j \frac{L_j^l i^{|l|-|l-m|-|m|} A_{j-n}^{l-m} A_n^m Y_{j-n}^{l-m}(\alpha_c, \beta_c) \lambda_c^{j-n}}{(-1)^{j+n} A_j^l} \quad (5.25)$$

with $r_c - r'_c = (\lambda_c, \alpha_c, \beta_c)$ and A_j^l like in Theorem 5.2.2.

Algorithm 4 The fast multipole method

```

// Compute the multipole expansion for every leaf-box
for boxes B on refinement level  $l_{\max}$  do
  Compute  $M_n^m$  for  $n = 0, \dots, p$  and  $m = -n, \dots, n$  centered at  $c_B$  for all particles
  contained in B after Equation 5.12 .
end for

// Compute the multipole expansion for every box
for  $l = l_{\max}, \dots, 2$  do
  for boxes B on refinement level  $l$  do
    Compute  $K_n^m$  for  $n = 0, \dots, p$  and  $m = -n, \dots, n$  centered at  $c_B$  after Equation 5.17
    resulting from all 8 subboxes of B and add them together.
  end for
end for

// Compute the local expansion of the far field for every box
for  $l = 2, \dots, l_{\max} - 1$  do
  for boxes A on refinement level  $l$  do
    Initialize the local expansion terms of A with the translated terms  $K_n^m$ 
    of As parent after Equation 5.25.
    for boxes B in interaction list of A do
      Compute  $L_n^m$  for  $n = 0, \dots, p$  and  $m = -n, \dots, n$  centered at  $c_A$ 
      after Equation 5.21 from the multipole expansion terms  $M_n^m$  of B
      and add them to the local expansion terms of A.
    end for
  end for
end for

// Assign far field and near interaction to actual particles
for boxes A on refinement level  $l_{\max}$  do
  Set the local expansion terms of A to the translated terms  $K_n^m$ 
  of As parent after Equation 5.25.
  for particles  $r_i$  in A do
    Assign the far field of  $r_i$  to  $\Phi(r_i)$  using the local expansion of A after Equation 5.20
    for particles  $r_j$  in near neighbors of A do
       $\Phi(r_i) \leftarrow \Phi(r_i) + q_j \frac{1}{|r_i - r_j|}$ 
    end for
  end for
end for

```

Here, we only rewrite a truncated series expansion inside its region of convergence. The error bounds from Theorem 5.2.3 are thus still valid. The operation count for one of these translations is again $O(p^4)$. Let us summarize the resulting algorithm, the fast multipole method, in Algorithm 4.

Finally, this is the original fast multipole method. As the number of terms p is derived from the required precision ε , it is fixed. Of course, the actual runtime heavily depends on constant factors like p and the number of boxes in an interaction list and a few comments are necessary. First of all, the number of p^2 terms needed as a compact representation both for multipole and for the local expansion and the resulting effort for translation and conversion of multipole into local expansion of p^4 can be quite high depending on p . Also, the interaction list of up to 189 boxes is larger than for example in two dimensions. The most crucial computational bottleneck however is the rate of decay of the approximation error. The multipole expansion leads to a worst case rate of decay of $(\sqrt{3}/3)^p$ but for the local expansion we can only assume about $(\frac{3}{4})^p$. This is because we need to consider the smallest distance between the two balls enclosing two boxes A and B where B is in A's interaction list. For the multipole expansion the distance between the ball enclosing B and the box A itself sufficed.

There are different approaches handling this complication. The original fast multipole method[69] not only excluded near neighbors from the interaction list but also second near neighbors, i.e. the near neighbors of near neighbors. Although this leads to an increased distance and therefore a better rate of decay for the error bound in p , there are now up to 125 near and second near neighbors and the interaction list grows up to 875 entries. Newer approaches try to reduce the high cost for the multipole to local conversion. For example, one can rotate the coordinate system, convert the expansion and then rotate back to the original system making use of a simpler conversion along the z -axis. Later approaches combine multipole expansion with plane wave expansion.[72]

In many applications and especially in the context of the BEM-FMM we are not only interested in the electric potential Φ but also the electric field. We need to compute the gradient field of Φ as well. Fortunately, we need not rely on numerical differentiation as we have expressed the far field as a local expansion in Equation 5.20. Partial derivatives of the terms are available analytically and additionally we obtain error bounds for $\nabla\Phi$ of exactly the same form as for Φ .

This concludes the chapter on the fast multipole method. The FMM library currently used in the BEM-FMM implementation is that of the Flatiron Institute and further information can be found in its documentation.[76]

Chapter 6

Comparison Studies of DUNEuro and BEM-FMM

Early numerical approaches to the forward problem were based on boundary element methods, see for example [59]. Different formulations have been derived since then, for example the mono- and double layer BEM and the symmetric BEM. Most BEM approaches are based on the assumption that the head is an isotropic volume conductor with nested shells of homogeneous tissues. Although modifications of these approaches for more complicated geometries do exist, finite element methods were introduced as they easily allow for arbitrary geometries with isotropic or even anisotropic conductivity. One drawback used to be the higher computational effort of FEM in comparison with BEM. This prevented the use of FEM as a realistic alternative to BEM until the early 2000s. An overview, evaluation and discussion of many boundary and finite element approaches can be found in [13]. Comparison studies of different BEM and FEM approaches followed, see for example [37, 77, 78].

In this work, we have seen a new boundary element formulation, the BEM-FMM. This method is presented as an alternative to FE methods that is able to deal with complicated geometries in recent publications. Comparison studies with different finite element implementations were concluded as showing good results.[56, 53, 57, 79].

Before we compare BEM-FMM with DUNEuro with different testbeds, we first summarize a few differences of theoretical nature. Of course, the boundary element method BEM-FMM is surface-based while the finite element implementation DUNEuro is volume-based. This results in large DUNEuro stiffness matrices as opposed to the system matrix of BEM-FMM. For example, in a multi-layer sphere model with realistic mesh resolution (see the first comparison) the FEM matrix has 222 thousand degrees of freedom while the BEM matrix only has 163 thousand. Of course, this imbalance is mitigated when we move to a realistic head geometry. The folded structure of the brain results in more surface area and thus more degrees of freedom for the BEM-FMM matrix. It has 841 thousand degrees of freedom for the model of the second study while the FEM matrix has 848 thousand. It is important to note that the latter is very sparse while we can not expect the former to have any zero entries. For example, DUNEuro reports only 12.5 million non-zero entries in the second study. We add that in both cases the matrices are never actually constructed but are applied as matrix-free operators. The fast multipole method is what drives this operation at the core of BEM-FMM and speeds up the computation.

We apply linear ansatz functions in DUNEuro while only constant ansatz functions are used in BEM-FMM. It is reported that the latter corresponds to the former and no accuracy is lost as one solves for the potential and the other for the charge distribution.[56] It should be noted that the current implementation of BEM-FMM is in MATLAB and does not include highly optimized linear solvers, preconditioners, parallelization and vectorization like the computationally efficient C++ code of DUNEuro does. In this aspect, we expect an advantage of DUNEuro and the underlying well-developed and maintained DUNE library. The FMM library on the other hand, which sits at the core of BEM-FMM, is efficiently implemented in FORTRAN and does make use of parallelization and vectorization.

Information on the DUNEuro toolbox, download, compilation, and usage can be found in [11]. A version of the direct BEM-FMM approach can be found on GitHub under [67] and an example using the reciprocity approach at [68]. As all studies were run on an OS with a Linux-kernel, we had to recompile the FMM implementation from [76] and used the “FAST_KER” option. Experiments were run on a machine with 80 Intel Xeon Gold 6148 processors running at 2.4 GHz. If not stated otherwise, all methods have been given access to all 80 cores.

Two difference measures are used. As we are interested in the EEG measurements and will make use of the transfer matrix and the reciprocity approach respectively, we only need to compare potential vectors representing the voltages at the electrodes. Of course, the same reference electrode must be used for the methods in question.

Definition 6.0.1 (Relative difference measure). *The relative difference measure (RDM) between two potential vectors V, V' is defined as*

$$RDM(V, V') = 50 \left\| \frac{V}{\|V\|_2} - \frac{V'}{\|V'\|_2} \right\|_2. \quad (6.1)$$

The RDM measures the potential distribution difference. As both vectors are normalized, the magnitude does not play a role. Only the distribution of potential at the evaluation points which the entries of V, V' represent is compared. It is scaled by 100 and divided by 2 and is thus stated in percent in a range between zero and 100. The optimal value, if and only if both potential vectors are the same, is zero.

Definition 6.0.2 (Magnitude measure). *The magnitude measure (MAG) between two potential vectors V, V' is defined as*

$$MAG(V, V') = \log\left(\frac{\|V\|_2}{\|V'\|_2}\right). \quad (6.2)$$

The magnitude measure is the complement to the RDM. It only measures the relative difference in magnitude between the two potential vectors. It is symmetric around zero and unbounded to both sides. The optimal value is zero.

In the following, we will look at two comparison studies. The first was conducted using a multi-layer sphere model while the second was computed on a realistic head model.

6.1 A Multi-layer Sphere Model

The first comparison study of BEM-FMM and DUNEuro is conducted on a multi-layer sphere model. We assume the head to consist of layered, nested, concentric, non-touching spheres of different tissues with homogeneous and isotropic conductivities per layer. Of course, it does not take into consideration effects of the complicated geometry of the brain, but it is a popular testbed as an analytical solution to the forward problem does exist for this case. The method described in [80] is implemented in the BEM-FMM software and was used to compute analytical solutions both numerical solutions could be compared with. Four layers of spheres of different radii represent brain, cerebrospinal fluid (CSF), skull, and skin, each with a different conductivity. Figure 6.1 illustrates this while Table 6.1 shows the specifications. This 4-layer sphere model is adopted for example from [24].

Compartment	Radius (mm)	Conductivity (S/m)
Brain	78	0.33
CSF	80	1.79
Skull	86	0.01
Scalp	92	0.43

Table 6.1: A spherical multilayer head model.

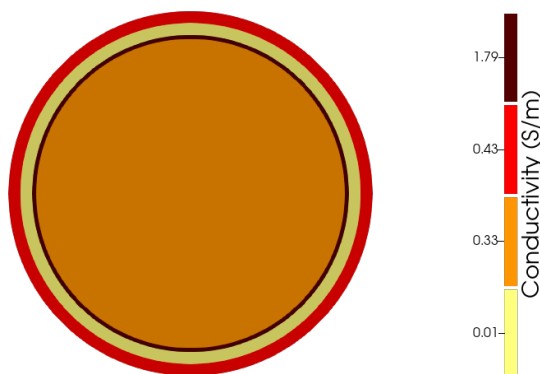


Figure 6.1: Illustration of the 4-layer sphere model and the conductivities of the different tissues.

We created this sphere model in the scripting language of the open source 3D finite element mesh generator Gmsh[81] and exported two- and three-dimensional simplicial meshes. The meshing process first computes triangulations of the boundaries between the layers as well as of the outer boundary before the tetrahedralization. This means that the triangles computed as surface meshes at the tissue boundaries are facets of tetrahedra on both sides and there is a coupling between surface and volume meshes. Different mesh resolutions were requested in order to investigate and compare convergence of the approaches at hand. The quality of the meshes was assessed with DistMesh[82]. It computes the radius of the largest circle contained in a triangle or tetrahedron and that of the smallest circumscribed circle. The quality measure is the ratio of these two radii and is scaled so that the optimal value is 1 while the lower bound is 0. Table 6.2 contains more information about the meshes. Both edge length and quality were averaged over all elements contained in the respective mesh. Figure 6.2 shows the surface mesh of the skin layer at resolutions corresponding to the first and third data column in the table.

#Vertices 2D	11007	21157	42185	81355	155734	347050	779874
#Triangles	21998	42298	84354	162694	311452	694084	1559732
#Vertices 3D	16037	34437	94223	222009	555289	1814373	6025120
#Tetrahedra	86110	187442	527617	1260507	3194545	10594864	35533997
Edge Length 2D	6.1306	4.4188	3.1283	2.2521	1.6277	1.0900	0.7271
Edge Length 3D	7.2110	5.6161	3.9577	2.9886	2.1892	1.4684	0.9828
Quality 2D	0.9843	0.9882	0.9896	0.9913	0.9919	0.9933	0.9939
Quality 3D	0.8029	0.8081	0.8343	0.8305	0.8379	0.8417	0.8446

Table 6.2: Details about the 4-layer sphere meshes.

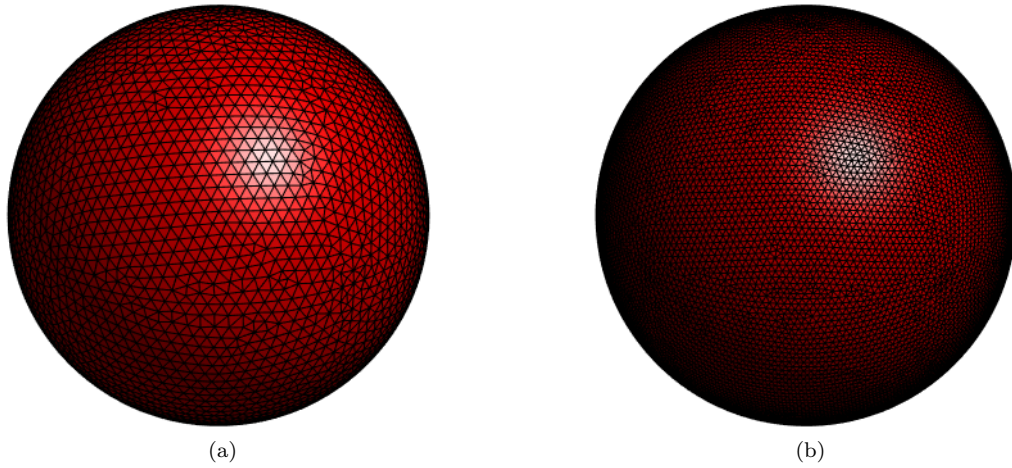


Figure 6.2: Different resolutions of skin surface meshes corresponding to first and third column in Table 6.2.

Next, a realistic number of 75 electrodes[83, 84] was distributed on the outermost surface. These can be seen imprinted on the skin surface by the BEM-FMM software in Figure 6.3. They are approximately equi-distant from each other and were created using [85]. We considered sets of dipolar sources at different radii, as the forward problem is more complicated to solve when the source is close to a conductivity boundary. The eccentricity of a source is measured as the ratio of the radius the source is located at and the radius of the boundary between brain and CSF. At each eccentricity presented in Table 6.3 we placed sets of 1.000 sources, once radial and once tangential. Per set, the sources have been distributed uniformly at random using [86] in order to rule out advantages for any method. Unit magnitude was assigned to each dipole.

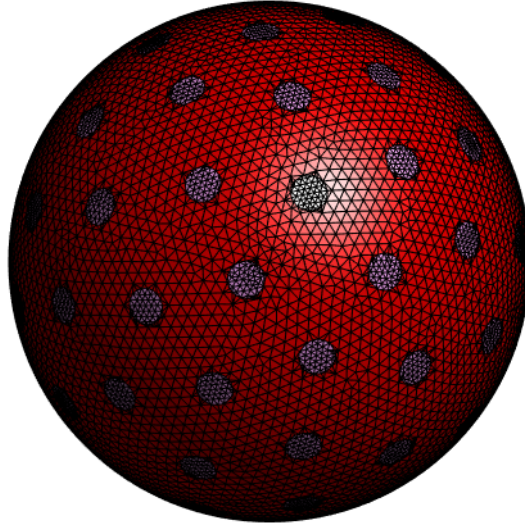


Figure 6.3: Triangles on the skin surface are assigned to electrodes by BEM-FMM.

Radius	8	28	48	68	73	74	75	76	77	77.5	77.75
Seperation	70	50	30	10	5	4	3	2	1	0.5	0.25
Eccentricity	0.1	0.36	0.62	0.87	0.94	0.95	0.962	0.974	0.987	0.9936	0.9968

Table 6.3: Radius, separation and eccentricity of the sets of sources.

In this study, a high number of sources in comparison with electrodes has been used. Thus, the transfer matrix and the reciprocity approach were applied. The DUNEuro linear solver was supplied with the following parameters.

```
maxit = 1000
reduction = 1e-14
```

Listing 6.1: DUNEuro linear solver parameters

We have used the following additional parameters for the Saint Venant approach implemented in DUNEuro. More information on these can be found at [87].

```

numberOfMoments=3
referenceLength=20
weightingExponent=1
relaxationFactor=1e-6
mixedMoments=True
restrict=True
initialization=closest_vertex

```

Listing 6.2: Saint Venant parameters

We have also included the parameters for BEM-FMM. Explanations are given as comments.

```

% Parameters for linear system Ac = b
is_refine_electrodes = true; % Refine triangles belonging to electrodes
is_refine_inner_shells = true; % Refine brain and CSF shells
TnumberE = 16; % Number of near neighbors on same shell for field
GnumberE = 0; % Number of near neighbors on other shells for field
RnumberP = 4; % Number of near neighbors on all shells for potential
iter = 35; % Maximum number of GMRES iterations
relres = 1e-12; % Minimum relative residual of GMRES
prec_charge = 1e-4; % Precision of FMM for solving for charge distribution
weight = 0.5; % Weight of conservation law

% Parameters for resulting application of reciprocity in order to derive potential
R = 0; % No precise integration for computation of field for reciprocity
prec_potential = 1e-4; % Precision of FMM for computation of field for reciprocity

```

Listing 6.3: BEM-FMM parameters

The finest mesh was not computationally feasible using these parameters and we turned off mesh refinement at the electrode triangles only for this mesh. We note that the mesh refinement for the brain and CSF shells as well as the refinement at the electrodes results in a bigger linear system than the number of triangles of the mesh given as input. For example, this procedure resulted in an increase from 163 thousand to 385 thousand triangles for the fourth mesh.

Figure 6.4 shows boxplots of the RDM for sources at a 2mm distance from CSF. Given a forward problem solver, the RDM was computed for each dipole by comparing the vectors containing the potential at the electrodes computed once with the analytical formula and once with the solver at hand. As a set of 1.000 dipoles is used per eccentricity and orientation, this results in 1.000 RDMs. The statistical distribution of these is then illustrated as one boxplot. Figure 6.4a is concerned with radial sources, while Figure 6.4b shows tangential dipoles. Both graphics show the mesh resolution, i.e. the average edge length, in mm on the x-axis. Note that the y-axis uses a logarithmic scale.

As expected from previous comparison studies, the Saint Venant approach produces smaller RDM errors than the partial integration source model. Most notable is the fact that BEM-FMM outperforms both DUNEuro FEM approaches for finer, more realistic meshes with regard to both median and spread of RDM. The sources are located at only 2mm distance from CSF while RDMs around 1% are achieved by all methods for meshes with an average edge length of 4mm. We observe that the DUNEuro approaches seem to be more stable for coarser meshes. Remember that mesh refinement is employed by the BEM-FMM reducing the average edge length approximately by a factor of 0.5. This needs to be taken into account when evaluating the figures as we see the mesh resolution of the input mesh and not the refined mesh on the x-axis. These observations are valid for both radial and tangential sources. Comparing the two figures, one

can note slightly better results of DUNEuro for tangential sources and of radial sources for BEM.

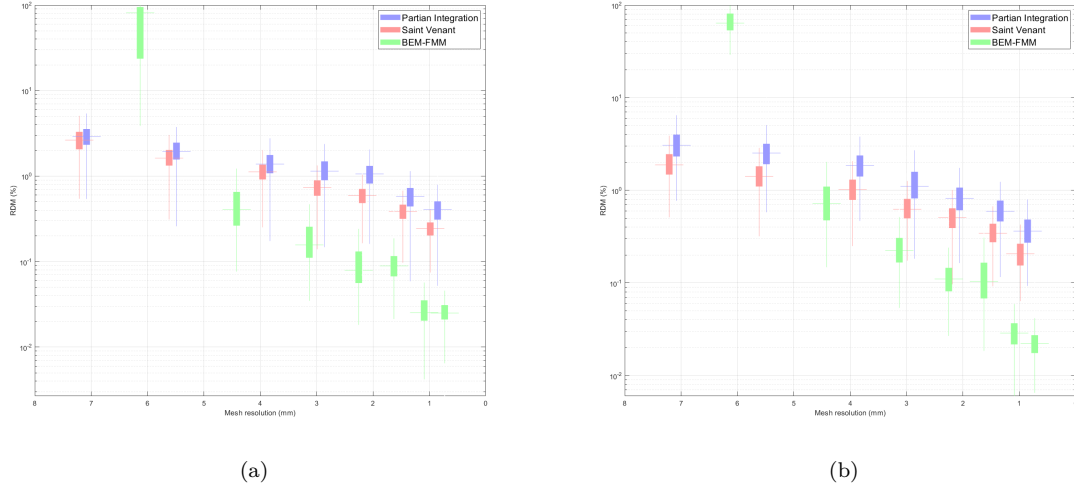


Figure 6.4: Boxplots of RDM over mesh resolution for sources at a 2mm distance from CSF: (a) radial sources and (b) tangential sources.

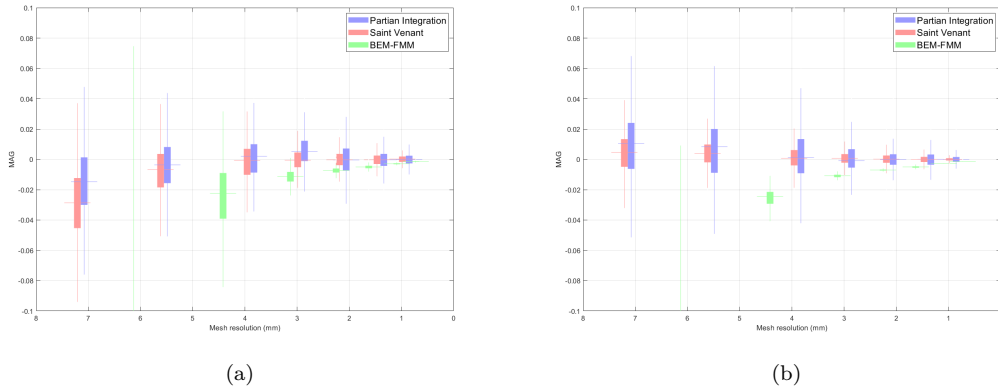
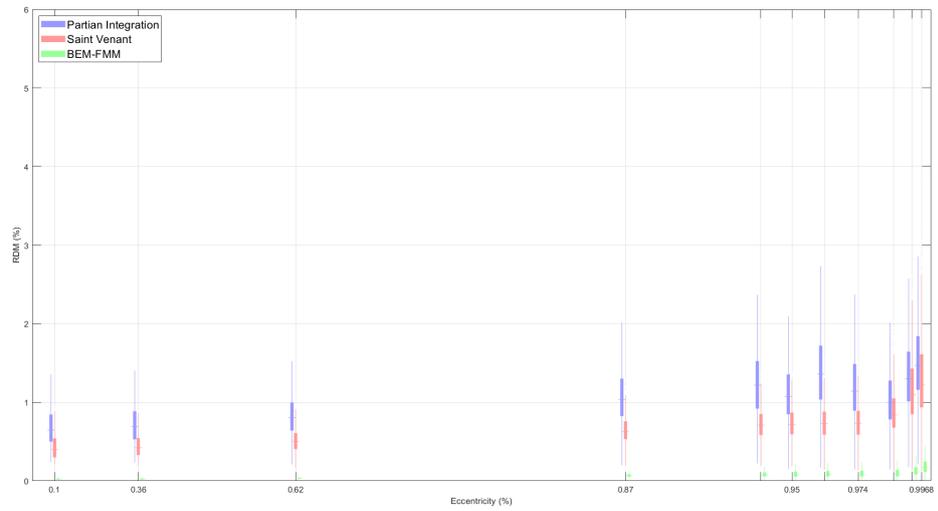
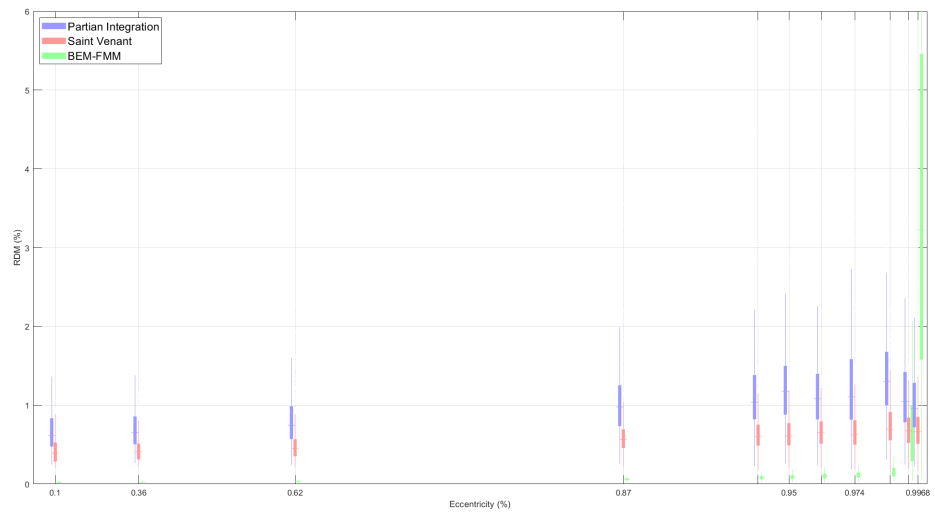


Figure 6.5: Boxplots of MAG over mesh resolution for sources at a 2mm distance from CSF: (a) radial sources and (b) tangential sources.

Figure 6.5 shows boxplots of the MAG for sources at a 2mm distance and was created with the same procedure as Figure 6.4. No logarithmic scaling has been used on the y-axis as it is inherent with our definition of the MAG. First, we note that both DUNEuro source models show less magnitude errors than the BEM-FMM regardless of mesh resolution. This is especially true for the median magnitude error indicated by horizontal lines while we do observe a wider statistical distribution, i.e. longer boxes for the DUNEuro MAGs than for the BEM-FMM results. Once again, DUNEuro seems to handle coarse meshes better than BEM-FMM. For fine meshes, both methods show good results and are in good agreement.



(a)

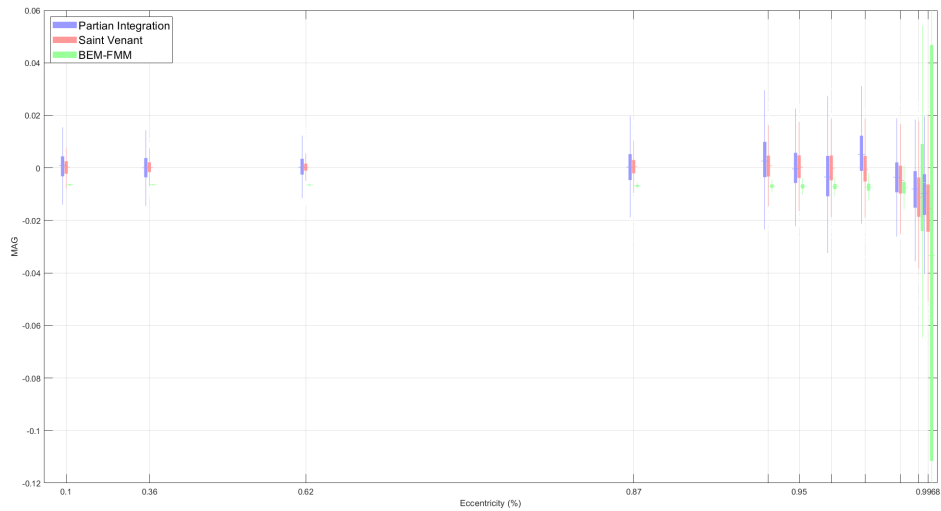


(b)

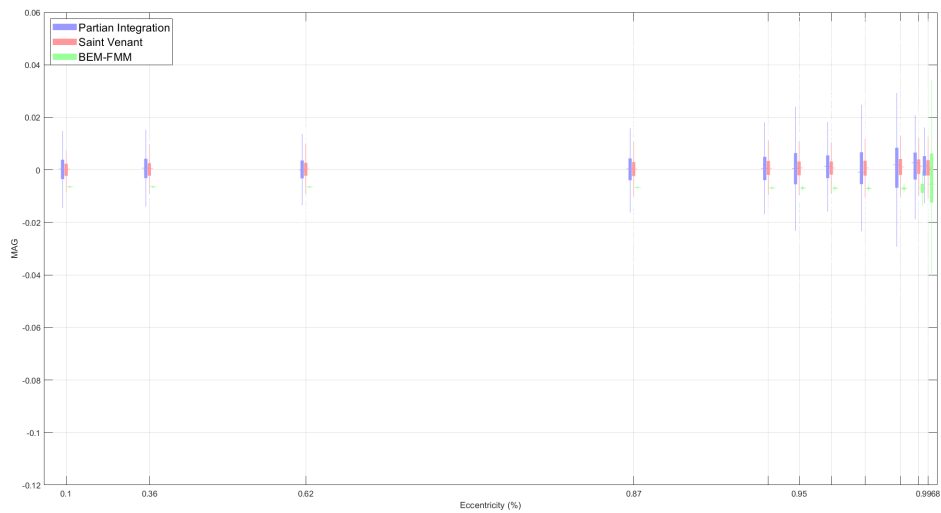
Figure 6.6: Boxplots of RDM over source eccentricity for fourth mesh resolution: (a) radial sources and (b) tangential sources.

In Figure 6.6 we can see boxplots of the RDM error for the fourth mesh in Table 6.2. The RDM was computed over the potential at the 75 electrodes per source and the boxplots then show the distribution of these RDMs over a set of 1.000 dipoles at a given eccentricity. This eccentricity, indicating the ratio of distance to CSF and radius of the brain/CSF boundary, is shown on the x-axis. Each marker on the axis corresponds to an eccentricity in Table 6.3.

Similar to Figure 6.4, we note that the RDM errors are smaller for the BEM-FMM than for the DUNEuro approaches approximately by the order of 10^{-1} . All three show sub-percentage accuracy, for higher eccentricity it is below 2%. The BEM-FMM is more sensitive to eccentricity than the DUNEuro approaches for tangential sources. The DUNEuro RDMs show a wider statistical spread, especially the partial integration approach.



(a)



(b)

Figure 6.7: Boxplots of MAG over source eccentricity for fourth mesh resolution: (a) radial sources and (b) tangential sources.

In Figure 6.7, we see boxplots of the MAG error for the fourth mesh. Again, we note that both DUNEuro approaches perform better than the BEM-FMM. They show a wider statistical spread but the magnitude errors are close to the optimal value of zero. Both approaches show more sensitivity to eccentricity for radial than for tangential sources. This is especially true for the BEM-FMM. We observe a high sensitivity for this boundary element method as compared to the two FEM approaches.

In conclusion, we observe that the BEM-FMM outperforms both DUNEuro approaches with regard to RDM errors while the opposite is true for the MAG. The boxes representing the DUNEuro solvers show a wider spread of errors. Both finite element methods are more stable with regard to coarse meshes and high eccentricities than the BEM-FMM. The latter can be explained as the volume-based approaches put a lot of effort and focus on dealing with the singular sources. We summarize that all approaches show good results, for example nearly sub-percent accuracy for the RDM. These may already be good enough depending on the application of the forward problem as other (physical) error sources like for example the imaging process, segmentation and conductivity will also contribute to the final solution. Of course, many of the advantages and reasons for the introduction of finite element methods really come into play with more realistic head geometries. Even though an analytical solution to compare with is then missing, a study with a realistic head model is of great interest.

Finally, we would also like to compare the performance of the approaches with regard to runtime. Figure 6.8 shows three plots of computation time in seconds over the average edge length of the mesh in mm. Figure 6.8a shows the total time including data import, preprocessing, iterative solver for the linear system and computation of the resulting potential at the 75 electrodes for one set of 1.000 radial sources located at 2mm from CSF. We note that most of the computational aspects are independent of the choice of sources. Only the set-up of the right-hand sides in DUNEuro and the application of the reciprocity approach in the BEM-FMM actually depend on the source. The computational effort of these last steps is approximately the same for sources at different eccentricities or with different orientations, especially when a total of 1.000 sources are considered. Figure 6.8b excludes the time it takes the BEM-FMM to refine the mesh at the electrodes and to imprint them onto the mesh. In Figure 6.8c we see the time it takes the three implementations to solve the linear system for the 75 electrodes and to compute the resulting potential for the same 1.000 sources. Thus, the time it takes DUNEuro to import the mesh and the BEM-FMM to do mesh refinement, imprint the electrodes and pre-compute more precise integral terms PC and EC is excluded. Note that the y-axis is scaled logarithmically.

Looking at the total computation time in Figure 6.8a, we see that the BEM-FMM runs for an extensively longer period than both DUNEuro approaches. If the input mesh refinement is chosen so that RDM and MAG errors are reasonable, the boundary element method takes around 15 minutes. At a mesh resolution of 2mm to 1mm average edge length, computation-time is around 3 hours and even goes up to 7 hours for the finest mesh (with electrode refinement turned off). Meanwhile, both DUNEuro source models take under 15 minutes for all except the finest mesh. The Saint Venant approach runs longer than the partial integration approach as the computation of the right-hand side vector is more intricate and thus costly, especially for 1.000 sources.

The refinement of the mesh around the electrodes in the BEM-FMM is computationally very expensive as an investigation into the long total runtime has shown and could possibly be improved by replacing the current MATLAB implementation of the refinement process. Figure 6.8b illustrates the runtime of BEM-FMM without this step. Still, DUNEuro clearly is faster. This is also true when we compare the time it takes to solve the linear system and compute the resulting potential in Figure 6.8c.

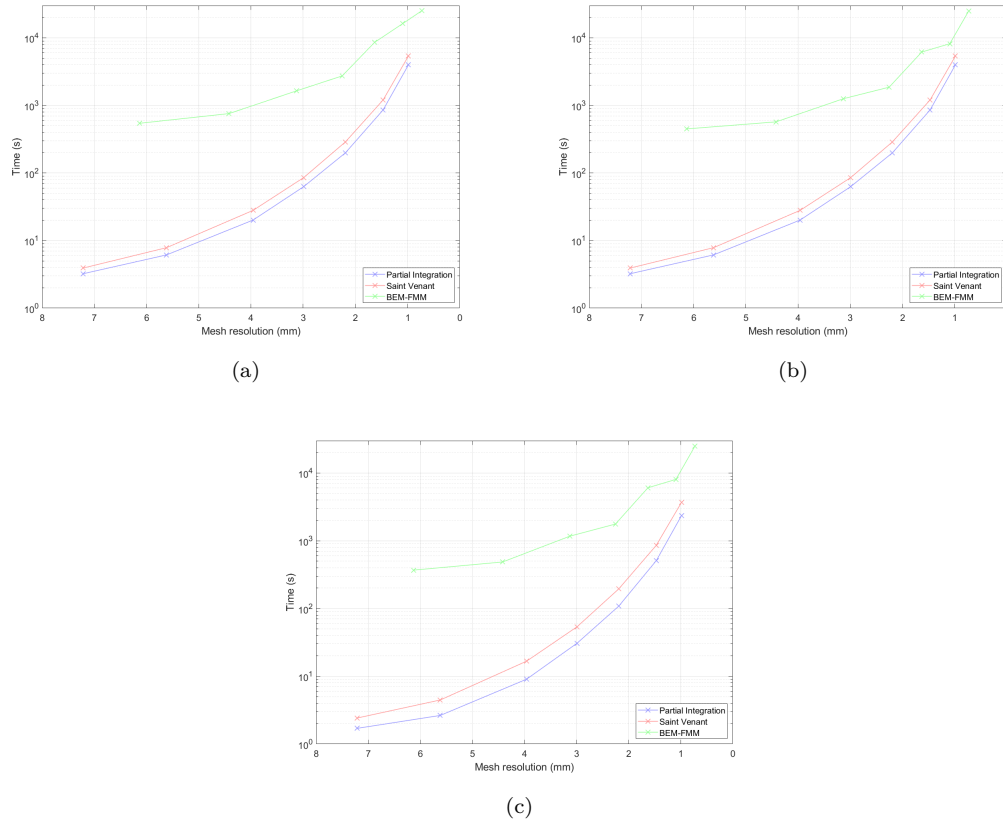


Figure 6.8: Plots of computation time over mesh resolution for radial sources at a 2mm distance from CSF: (a) Complete time (b) Complete time without electrode refinement for BEM-FMM (c) Time without “preprocessing”.

DUNEuro has some implementation advantages in its favour. First of all, DUNEuro is parallelized while the BEM-FMM engine itself is not. The fast multipole method library, which is called, makes use of parallelization and is responsible for one of the most costly computation steps, though. Next, DUNEuro is based on the DUNE framework and makes use of state-of-the-art preconditioners like an AMG preconditioner and iterative solvers. The C++ implementation DUNEuro is thus surely more optimized than the MATLAB BEM-FMM code. It will be interesting to investigate how a runtime comparison plays out if both are at an equal level of numerical and software optimization. One could then see more clearly advantages or disadvantages of the theoretical mathematical approaches behind the software.

6.2 A Realistic Head Model

We have adopted a scenario previously used in [55]. The corresponding code and data was made available at [67]. The third example is a realistic setup representing subject #110411 of Human Connectome Project[88] which was segmented with SimNIBS[89]. This third example was reused with minor modifications that will be presented. First, we have included the tissues as listed in Table 6.4 and illustrated in Figure 6.9.

Compartment	Conductivity (S/m)
White matter	0.126
Gray matter	0.275
CSF	1.654
Skull	0.010
Scalp	0.465

Table 6.4: A realistic head model.

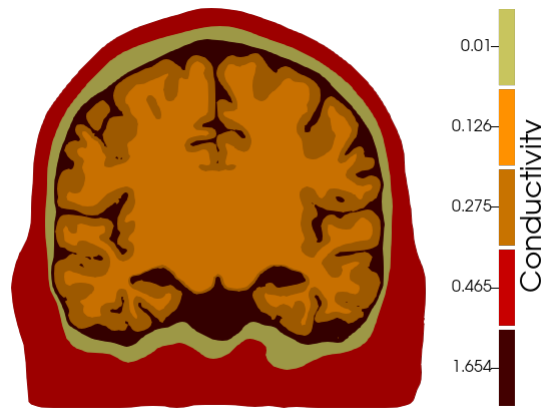


Figure 6.9: A slice of the realistic head model and the conductivities of the different tissues.

The triangular surface meshes included in the dataset (see Figure 6.10) were imported into Gmsh[81] and a tetrahedral volume mesh was created. The two meshes are thus connected in the sense that the tetrahedra facets at the tissue boundaries coincide with the triangles from the surface meshes. Table 6.5 lists the specifications of the two meshes.

#Vertices 2D	420745
#Triangles	841470
#Vertices 3D	848063
#Tetrahedra	4889216
Edge Length 2D	1.4591
Edge Length 3D	2.0146
Quality 2D	0.9413
Quality 3D	0.7961

Table 6.5: Details about the realistic head meshes.

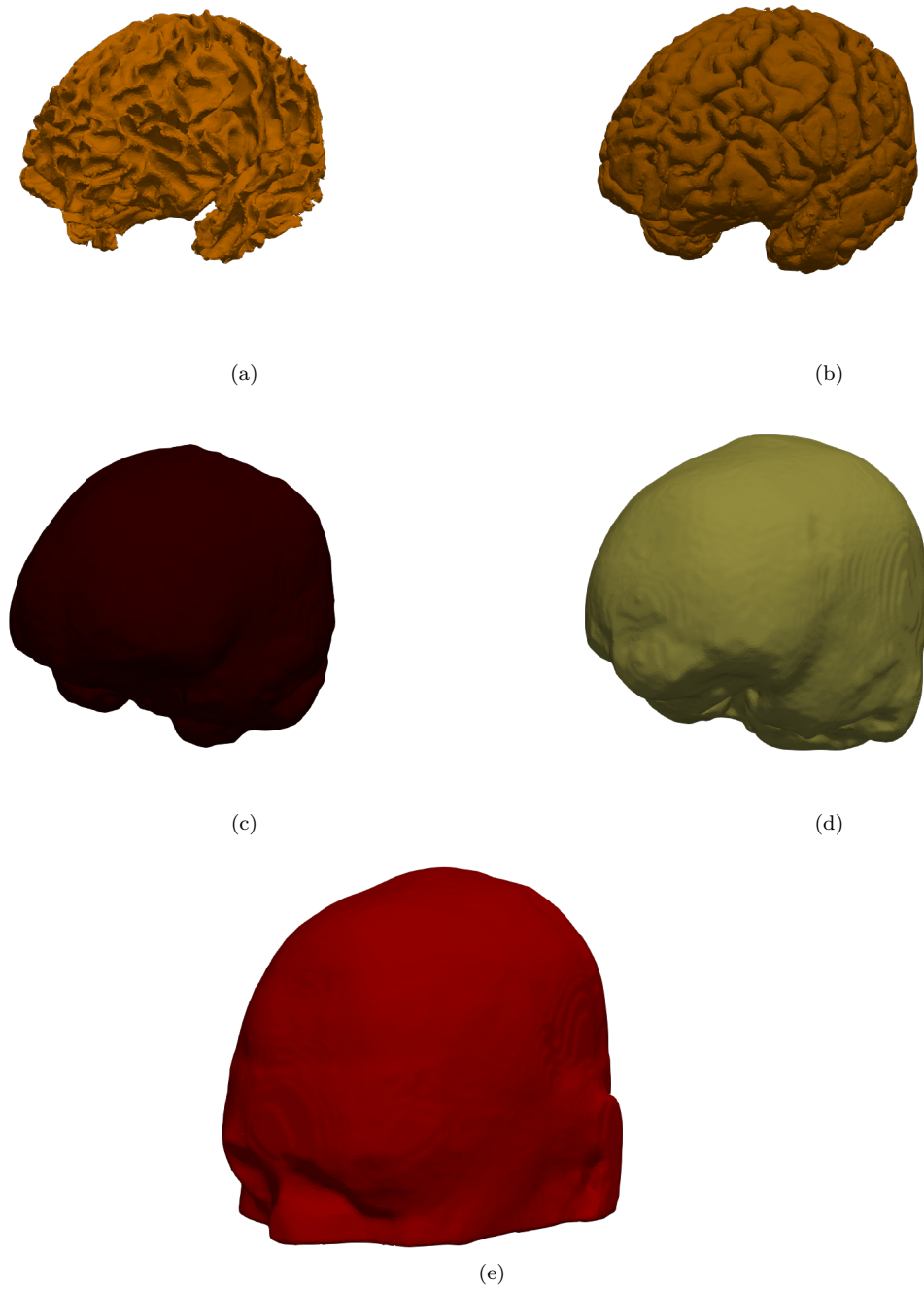


Figure 6.10: Compartments of the realistic head model shown from the front: (a) White matter (b) Gray matter (c) CSF (d) Skull (e) Scalp.

Next, the example code sets up a patch of radial dipoles. This is done by choosing a number of gray matter triangles. Then, their center points are computed and transposed by -2mm in the direction of the unit outer normals. We now have points lying 2mm inside the gray matter. Dipoles are set at these locations with the orientation of the same normals. We have restricted our comparison to the first of these dipoles (see Figure 6.11). Accordingly, we have not used the transfer matrix approach of DUNEuro. The direct source model is employed for the BEM-FMM. The remaining code from the exemplary GitHub repository is unaltered and the BEM-FMM parameters can be found there. For the Saint Venant approach we made use of the same parameters as for the multi-layer sphere model.

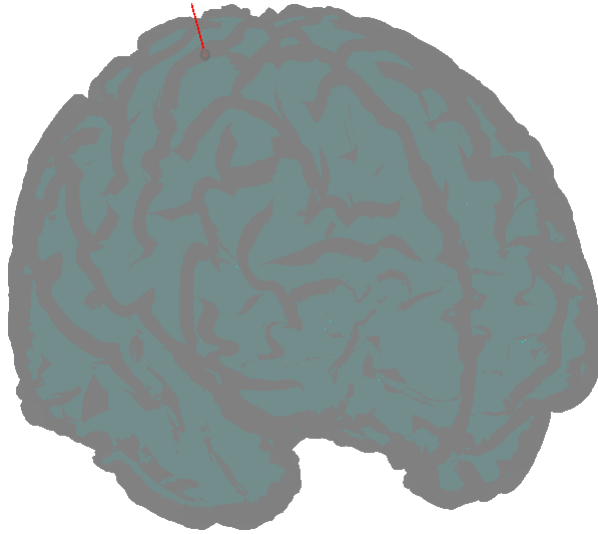


Figure 6.11: The dipole in the realistic head model. The gray matter is shown as transparent gray surface while the white matter is turquoise. The red arrow indicates the dipole at a visible scaling.

The BEM-FMM computes the resulting potential at all triangle centers of the mesh. The finite element methods of DUNEuro solve for the potential at the volumetric mesh nodes. We have implemented a method which then derives the potential at all centers of tetrahedra facets which lie on the skin surface. The results from both the BEM-FMM and the two DUNEuro approaches can thus be compared at all centers of skin surface triangles.

We have computed the RDM and MAG of the BEM-FMM and DUNEuro with the partial integration approach as well as of the BEM-FMM and DUNEuro with the Saint Venant approach. The results can be seen in Table 6.6.

	RDM (%)	MAG
Partial integration	4.078	0.2070
Saint Venant	4.550	0.1579

Table 6.6: Difference measures of results of the BEM-FMM and the DUNEuro approaches for the realistic head model.

We note that the potential distribution difference between the BEM-FMM and DUNEuro are around 4% for both DUNEuro source models. This is surely not the sub-percentage agreement we have seen with the multi-layer sphere model. A visual inspection of the potential distribution for the three solutions (Figure 6.12) shows us good agreement, nevertheless. We can also see in the figure that the magnitudes are not as far off as the MAGs in Table 6.6 might suggest when compared to the results in the previous study. One reason for this might be the high number of 119.990 evaluation points.

Additionally, we have measured the runtime of the three methods. Table 6.7 lists the total runtime and the runtime without “preprocessing”. This includes the import of the mesh for DUNEuro and as well as for the BEM-FMM the computation of PC and EC .

	Total time (s)	Time without “preprocessing” (s)
BEM-FMM	483	211
DUNEuro partial integration	187	65
DUNEuro Saint Venant	205	73

Table 6.7: Runtime of the BEM-FMM and the DUNEuro approaches for the realistic head model.

Once again, we note the efficiency of DUNEuro. BEM-FMM runs more than twice the time it takes DUNEuro to compute a solution even though parallelization is not a factor with only one dipole.

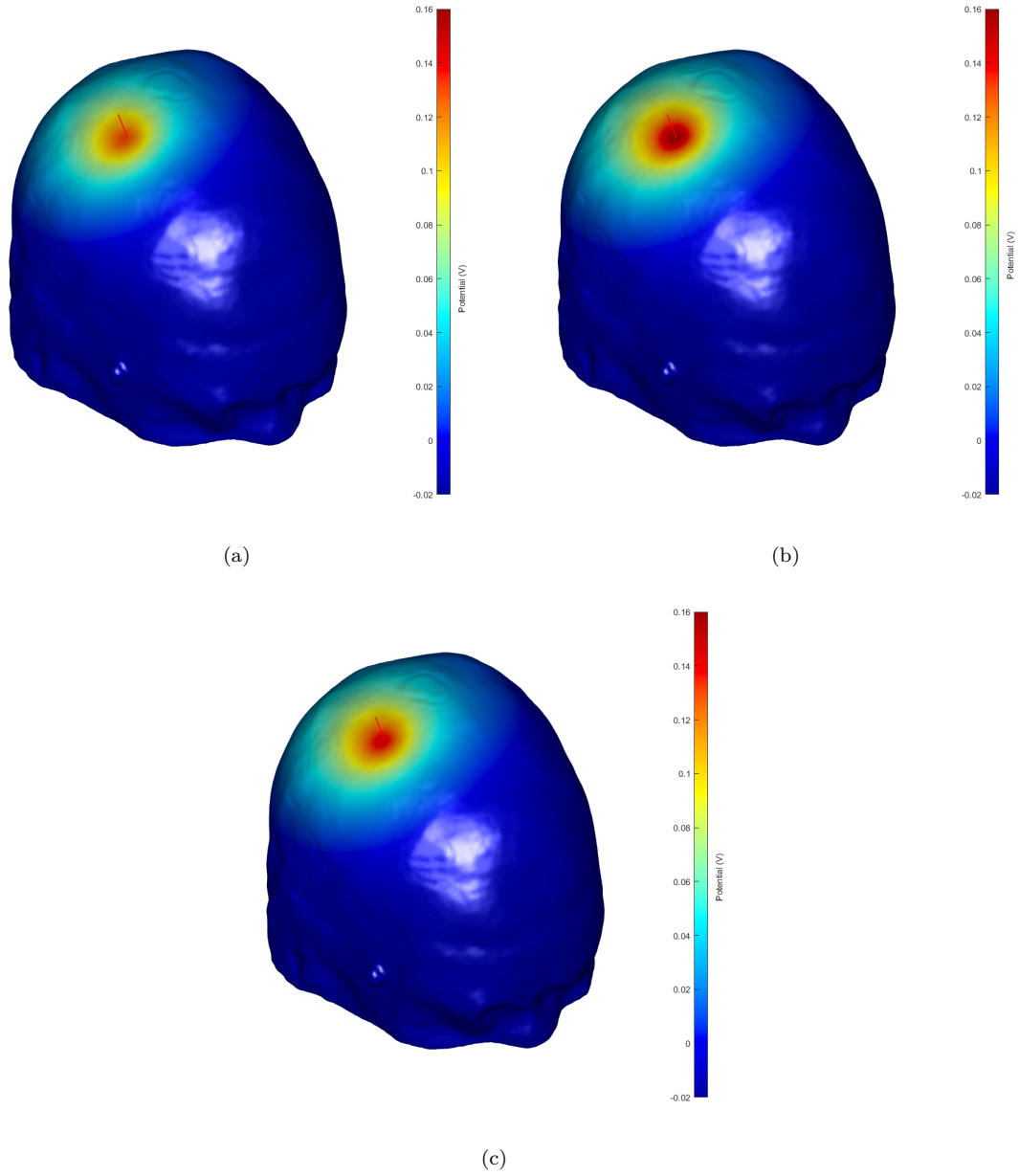


Figure 6.12: Visualization of the potential on the head surface produced by: (a) The BEM-FMM (b) The partial integration model (c) The Saint Venant model.

6.3 Conclusion and Outlook

In summary, the first study has shown that both approaches produce accurate results suitable for practical applications. This is especially true when we consider other sources of error for example in the modeling process. The second, realistic study shows agreement of the solutions but further investigation for example with other models and a reference method to compare with would be of great interest. One might also model non-nested tissues and conductivity anisotropy in order to test DUNEuro and BEM-FMM with more realistic models of higher complexity.

With regard to the runtime, we have seen a clear advantage of DUNEuro. There are a few ideas that come to mind about how to improve the efficiency of the BEM-FMM implementation. First, one could reimplement the approach in a more efficient programming language. A C++ implementation could be based on the DUNE framework allowing access to the state-of-the-art linear solvers and preconditioners and also features like parallelization.

The BEM-FMM reciprocity approach was introduced to shift the computational effort from the number of sources to the number of electrodes. This is similar to the DUNEuro transfer matrix approach. Instead, one could adapt the transfer matrix approach for the BEM-FMM as well. The basic idea is as follows. The BEM-FMM direct approach solves a linear system $Ac = b$. Then, c is used in order to compute the secondary potential following

$$\varphi^s(r_j) = \sum_{i=1}^n \left(\frac{1}{4\pi |r_j - r_i|} A_i + PC_j i \right) c_i. \quad (6.3)$$

Let r_{j_1}, \dots, r_{j_m} be the triangle centers we have located the electrodes at. We define

$$R_{ji} = \frac{1}{4\pi |r_j - r_i|} A_i + PC_j i \quad (6.4)$$

for $j = j_1, \dots, j_m$ and $i = 1, \dots, n$. As we have seen in Chapter 3.5, we can now solve the system $AT^t = R$ once and then compute the potential electrodes simply by using Tc . This also has the advantage that the matrix of the linear system $AT^t = R$ we would like to solve is independent of the electrodes. This is not the case with the BEM-FMM reciprocity approach. We are thus able to apply block Krylov solvers as they are presented for example in [20].

Of course, this transfer matrix approach for BEM-FMM needs to be further developed and the above is only a general outlook on what could be possible. In general, a thorough theoretical mathematical investigation into existence and uniqueness of solutions to both the integral equation and the resulting linear equation of BEM-FMM might be interesting. This also includes convergence results.

Bibliography

- [1] Michael S. Gazzaniga, Richard B. Ivry, and George R. Mangun. *Cognitive Neuroscience: The Biology of the Mind*. 4th ed. W. W. Norton & Company, 2014. ISBN: 978-0-393-91348-4.
- [2] Hans Hallez et al. “Review on solving the forward problem in EEG source analysis”. In: *Journal of NeuroEngineering and Rehabilitation* 4 (2007), pp. 46–46.
- [3] Wenyi Yan and Oscar Pangestu. “A modified human head model for the study of impact head injury”. In: *Computer methods in biomechanics and biomedical engineering* 14 (2011-07), pp. 1049–57. DOI: 10.1080/10255842.2010.506435.
- [4] Charles G. Stangor and Jennifer Walinga. *Introduction to Psychology - 1st Canadian Edition*. 2014. URL: <https://opentextbc.ca/introductiontopsychology/>.
- [5] Johannes Vorwerk. “Comparison of Numerical Approaches to the EEG Forward Problem”. Diploma Thesis. University of Münster, 2011.
- [6] R. Plonsey. “Action potential sources and their volume conductor fields”. In: *Proceedings of the IEEE* 65.5 (1977), pp. 601–611. DOI: 10.1109/PROC.1977.10539.
- [7] Matti Hämäläinen et al. “Magnetoencephalography—theory, instrumentation, and applications to noninvasive studies of the working human brain”. In: *Rev. Mod. Phys.* 65 (2 1993-04), pp. 413–497. DOI: 10.1103/RevModPhys.65.413. URL: <https://link.aps.org/doi/10.1103/RevModPhys.65.413>.
- [8] Shingo Murakami and Yoshio Okada. “Contributions of principal neocortical neurons to magnetoencephalography and electroencephalography signals”. In: *The Journal of physiology* 575 (2006-10), pp. 925–36. DOI: 10.1113/jphysiol.2006.105379.
- [9] Timo Kirschstein and Rüdiger Köhling. “What is the source of the EEG?” In: *Clinical EEG and neuroscience : official journal of the EEG and Clinical Neuroscience Society (ENCS)* 40 (2009-08), pp. 146–9. DOI: 10.1177/155005940904000305.
- [10] Jan De Munck, Bob Dijk, and Henk Spekreijse. “Mathematical Dipoles are Adequate to Describe Realistic Generators of Human Brain Activity”. In: *IEEE transactions on biomedical engineering* 35 (1988-12), pp. 960–6. DOI: 10.1109/10.8677.
- [11] Sophie Schrader et al. “DUNEuro—A software toolbox for forward modeling in bioelectromagnetism”. In: *PLoS ONE* 16 (2021-06). DOI: <https://doi.org/10.1371/journal.pone.0252431>.
- [12] J. Sarvas. “Basic mathematical and electromagnetic concepts of the biomagnetic inverse problem”. In: *Physics in Medicine and Biology* 32.1 (1987-01), pp. 11–22. DOI: 10.1088/0031-9155/32/1/004. URL: <https://doi.org/10.1088/0031-9155/32/1/004>.

- [13] Jan C. de Munck, Carsten H. Wolters, and Maureen Clerc. “EEG and MEG: forward modeling”. In: *Handbook of Neural Activity Measurement*. Ed. by Romain Brette and Alain Destexhe. Cambridge University Press, 2012, pp. 192–256. DOI: 10.1017/CB09780511979958.006.
- [14] James Clerk Maxwell. “A dynamical theory of the electromagnetic field”. In: 155 (1865), pp. 459–513.
- [15] Robert Plonsey and Dennis B. Heppner. “Considerations of quasi-stationarity in electrophysiological systems.” In: *The Bulletin of mathematical biophysics* 29 4 (1967), pp. 657–64.
- [16] Johannes Vorwerk et al. “A guideline for head volume conductor modeling in EEG and MEG”. In: *NeuroImage* 100 (2014), pp. 590–607. ISSN: 1053-8119. DOI: <https://doi.org/10.1016/j.neuroimage.2014.06.040>. URL: <https://www.sciencedirect.com/science/article/pii/S1053811914005175>.
- [17] Carsten Wolters et al. “Numerical Mathematics of the Subtraction Method for the Modeling of a Current Dipole in EEG Source Reconstruction Using Finite Element Head Models”. In: *SIAM J. Scientific Computing* 30 (2007-01), pp. 24–45. DOI: 10.1137/060659053.
- [18] Lawrence C. Evans. *Partial Differential Equations*. 2nd ed. Graduate studies in mathematics 19. American Mathematical Society, 2014.
- [19] Tuuli Miinalainen et al. “A realistic, accurate and fast source modeling approach for the EEG forward problem”. In: *NeuroImage* 184 (2019), pp. 56–67. ISSN: 1053-8119. DOI: <https://doi.org/10.1016/j.neuroimage.2018.08.054>. URL: <https://www.sciencedirect.com/science/article/pii/S1053811918307523>.
- [20] Malte Höltershinken. “Efficient Computation of Transfer Matrices using the Block Conjugate Gradient Method”. Master’s Thesis. University of Münster, 2021.
- [21] Dietrich Braess. *Finite Elements: Theory, Fast Solvers, and Applications in Solid Mechanics*. 3rd ed. Cambridge University Press, 2007. DOI: 10.1017/CB09780511618635.
- [22] F. Drechsler et al. “A full subtraction approach for finite element method based source analysis using constrained Delaunay tetrahedralisation”. In: *Neuroimage* 46.4 (2009), pp. 1055–65. DOI: <https://doi.org/10.1016/j.neuroimage.2009.02.024>. URL: <https://pubmed.ncbi.nlm.nih.gov/19264145/>.
- [23] Sophie Schrader et al. “DUNEuro—A software toolbox for forward modeling in bioelectromagnetism”. In: *PLOS ONE* 16.6 (2021-06). Ed. by Christos Papadelis, e0252431. ISSN: 1932-6203. DOI: 10.1371/journal.pone.0252431. URL: <http://dx.doi.org/10.1371/journal.pone.0252431>.
- [24] C. Engwer et al. “A Discontinuous Galerkin Method to Solve the EEG Forward Problem Using the Subtraction Approach”. In: *SIAM Journal on Scientific Computing* 39.1 (2017), B138–B164. DOI: 10.1137/15M1048392. eprint: <https://doi.org/10.1137/15M1048392>. URL: <https://doi.org/10.1137/15M1048392>.
- [25] Florian Grüne. “Validierung von FEM-Ansätzen höherer Ordnung für das EEG-Vorwärtsproblem”. Master’s Thesis. University of Münster, 2014.
- [26] Maria Carla Piastra et al. “A comprehensive study on electroencephalography and magnetoencephalography sensitivity to cortical and subcortical sources”. In: *Human Brain Mapping* 42.4 (2021), pp. 978–992. DOI: <https://doi.org/10.1002/hbm.25272>. eprint: <https://onlinelibrary.wiley.com/doi/pdf/10.1002/hbm.25272>. URL: <https://onlinelibrary.wiley.com/doi/abs/10.1002/hbm.25272>.

- [27] Maria Carla Piastra et al. *The WWU DUNEuro reference data set for combined EEG/MEG source analysis*. The research related to this dataset was supported by the German Research Foundation (DFG) through project WO1425/7-1 and the EU project ChildBrain (Marie Curie Innovative Training Networks, grant agreement 641652). Zenodo, 2020-06. DOI: 10.5281/zenodo.3888381. URL: <https://doi.org/10.5281/zenodo.3888381>.
- [28] S. Lew et al. “Accuracy and run-time comparison for different potential approaches and iterative solvers in finite element method based EEG source analysis”. In: *Applied Numerical Mathematics* 59.8 (2009), pp. 1970–1988. ISSN: 0168-9274. DOI: <https://doi.org/10.1016/j.apnum.2009.02.006>. URL: <https://www.sciencedirect.com/science/article/pii/S016892740900021X>.
- [29] Sampsa Pursiainen, Johannes Vorwerk, and Carsten Wolters. “Electroencephalography (EEG) Forward Modeling via H(div) Finite Element Sources with Focal Interpolation”. In: *Physics in medicine and biology* 61 (2016-08). DOI: 10.1088/0031-9155/61/24/8502.
- [30] M. Bauer et al. “Comparison Study for Whitney (Raviart–Thomas)-Type Source Models in Finite-Element-Method-Based EEG Forward Modeling”. In: *IEEE Transactions on Biomedical Engineering* 62.11 (2015), pp. 2648–2656. DOI: 10.1109/TBME.2015.2439282.
- [31] Carsten Wolters et al. “Numerical approaches for dipole modeling in finite element method based source analysis”. In: *International Congress Series* 1300 (2007-06), pp. 189–192. DOI: 10.1016/j.ics.2007.02.014.
- [32] Alberto Valli. “Solving an electrostatics-like problem with a current dipole source by means of the duality method”. In: *Applied Mathematics Letters* 25.10 (2012), pp. 1410–1414. ISSN: 0893-9659. DOI: <https://doi.org/10.1016/j.aml.2011.12.013>. URL: <https://www.sciencedirect.com/science/article/pii/S0893965911006082>.
- [33] Ana Alonso Rodríguez et al. “A posteriori error estimates for the problem of electrostatics with a dipole source”. In: *Comput. Math. Appl.* 68 (2014), pp. 464–485.
- [34] K.A. Awada et al. “Computational aspects of finite element modeling in EEG source localization”. In: *IEEE Transactions on Biomedical Engineering* 44.8 (1997), pp. 736–752. DOI: 10.1109/10.605431.
- [35] Helmut Buchner et al. “Inverse localization of electric dipole current sources in finite element models of the human head.” In: *Electroencephalography and clinical neurophysiology* 102 4 (1997), pp. 267–78.
- [36] Takfarinas Medani et al. “FEM Method for the EEG Forward Problem and Improvement Based on Modification of the Saint Venant’s Method”. In: *Progress in Electromagnetics Research* 153 (2015-10), pp. 11–22. DOI: 10.2528/PIER15050102.
- [37] Andreas Nüß. “Fitted and Unfitted Finite Element Methods for Solving the EEG Forward Problem”. Dissertation. University of Münster, 2018.
- [38] Carlotta Barkhau. “Evaluation of the Multipolar Venant Source Modeling Approach in EEG Source Analysis”. Master’s Thesis. University of Münster, 2021.
- [39] Anne Hanrath. “Finite Element Representation of the EEG Forward Problem with Multipole Expansion”. Dissertation. RWTH Aachen University, 2019.
- [40] Johannes Vorwerk et al. “The multipole approach for EEG forward modeling using the finite element method”. In: *NeuroImage* 201 (2019), p. 116039. ISSN: 1053-8119. DOI: <https://doi.org/10.1016/j.neuroimage.2019.116039>. URL: <https://www.sciencedirect.com/science/article/pii/S1053811919306202>.

- [41] Felix Lucka et al. “Hierarchical Bayesian inference for the EEG inverse problem using realistic FE head models: Depth localization and source separation for focal primary currents”. In: *NeuroImage* 61.4 (2012), pp. 1364–1382. ISSN: 1053-8119. DOI: <https://doi.org/10.1016/j.neuroimage.2012.04.017>. URL: <https://www.sciencedirect.com/science/article/pii/S1053811912003989>.
- [42] Carsten Wolters, Lars Grasedyck, and Wolfgang Hackbusch. “Efficient Computation of lead field bases and influence matrix for the FEM-based EEG and MEG inverse problem”. In: *Inverse Problems* 20 (2004-08), pp. 1099–1116. DOI: 10.1088/0266-5611/20/4/007.
- [43] F. Sharbrough et al. “American Electroencephalographic Society guidelines for standard electrode position nomenclature”. In: *Clinical Neurophysiology* 8 (1991-01), pp. 200–202.
- [44] Jayant Acharya et al. “American Clinical Neurophysiology Society Guideline 2: Guidelines for Standard Electrode Position Nomenclature”. In: *The Neurodiagnostic Journal* 56 (2016-10), pp. 245–252. DOI: 10.1080/21646821.2016.1245558.
- [45] Peter Bastian et al. “The Dune framework: Basic concepts and recent developments”. In: *Computers & Mathematics with Applications* 81 (2021). Development and Application of Open-source Software for Problems with Numerical PDEs, pp. 75–112. ISSN: 0898-1221. DOI: <https://doi.org/10.1016/j.camwa.2020.06.007>. URL: <https://www.sciencedirect.com/science/article/pii/S089812212030256X>.
- [46] Z.-S Chen, Holger Waubke, and Wolfgang Kreuzer. “A formulation of the fast multipole boundary element method (FMBEM) for acoustic radiation and scattering from three-dimensional structures”. In: *Journal of Computational Acoustics* 16 (2008-06). DOI: 10.1142/S0218396X08003725.
- [47] Haijun Wu, Yijun Liu, and Weikang Jiang. “A fast multipole boundary element method for 3D multi-domain acoustic scattering problems based on the Burton–Miller formulation”. In: *Engineering Analysis with Boundary Elements* 36.5 (2012), pp. 779–788. ISSN: 0955-7997. DOI: <https://doi.org/10.1016/j.enganabound.2011.11.018>. URL: <https://www.sciencedirect.com/science/article/pii/S0955799711002645>.
- [48] J. Song, Cai-Cheng Lu, and Weng Cho Chew. “Multilevel fast multipole algorithm for electromagnetic scattering by large complex objects”. In: *IEEE Transactions on Antennas and Propagation* 45.10 (1997), pp. 1488–1493. DOI: 10.1109/8.633855.
- [49] W.C. Chew et al. *Fast and Efficient Algorithms in Computational Electromagnetics*. USA: Artech House, Inc., 2001. ISBN: 1580531520.
- [50] Jan Kybic et al. “Fast multipole acceleration of the MEG/EEG boundary element method”. In: *Physics in Medicine and Biology* 50.19 (2005-09), pp. 4695–4710. DOI: 10.1088/0031-9155/50/19/018. URL: <https://doi.org/10.1088/0031-9155/50/19/018>.
- [51] Jens Haueisen et al. “Neuromagnetic field computation using the multiple multipole method”. In: *International Journal of Numerical Modelling-electronic Networks Devices and Fields - INT J NUMER MODEL ELECTRON N* 9 (1996-01), pp. 145–158. DOI: 10.1002/(SICI)1099-1204(199601)9:1/23.3.CO;2-L.
- [52] G. Of, Olaf Steinbach, and W. L. Wendland. “A fast multipole boundary element method for the symmetric boundary integral formulation”. English. In: *Proceedings of IABEM 2002*. 2002.
- [53] Sergey N. Makarov et al. “Boundary element fast multipole method for modeling electrical brain stimulation with voltage and current electrodes”. In: *Journal of Neural Engineering* 18.4 (2021-08), p. 0460d4. DOI: 10.1088/1741-2552/ac17d7. URL: <https://doi.org/10.1088/1741-2552/ac17d7>.

- [54] S. N. Makarov et al. “Boundary Element Fast Multipole Method for Enhanced Modeling of Neurophysiological Recordings”. In: *IEEE Transactions on Biomedical Engineering* 68.1 (2021), pp. 308–318. DOI: 10.1109/TBME.2020.2999271.
- [55] Sergey N Makarov et al. “A software toolkit for TMS electric-field modeling with boundary element fast multipole method: an efficient MATLAB implementation”. In: *Journal of Neural Engineering* 17.4 (2020-08), p. 046023. DOI: 10.1088/1741-2552/ab85b3. URL: <https://doi.org/10.1088/1741-2552/ab85b3>.
- [56] Sergey N. Makarov et al. “A Quasi-Static Boundary Element Approach With Fast Multipole Acceleration for High-Resolution Bioelectromagnetic Models”. In: *IEEE Transactions on Biomedical Engineering* 65.12 (2018), pp. 2675–2683. DOI: 10.1109/TBME.2018.2813261.
- [57] A. T. Htet et al. “Comparative performance of the finite element method and the boundary element fast multipole method for problems mimicking transcranial magnetic stimulation (TMS)”. In: *Journal of Neural Engineering* 16.2 (2019-02), p. 024001. DOI: 10.1088/1741-2552/aafbb9. URL: <https://doi.org/10.1088/1741-2552/aafbb9>.
- [58] V. S. Vladimirov. *Equations of Mathematical Physics*. Marcel Dekker, New York, 1971.
- [59] A.C. L. Barnard, I.M. Duck, and M.S. Lynn. “The Application of Electromagnetic Theory to Electrocardiology: I. Derivation of the Integral Equations”. In: *Biophysical Journal* 7.5 (1967), pp. 443–462. ISSN: 0006-3495. DOI: [https://doi.org/10.1016/S0006-3495\(67\)86598-6](https://doi.org/10.1016/S0006-3495(67)86598-6). URL: <https://www.sciencedirect.com/science/article/pii/S0006349567865986>.
- [60] Jaakko Malmivuo and Robert Plonsey. *Bioelectromagnetism - Principles and Applications of Bioelectric and Biomagnetic Fields*. 1995-10. ISBN: 978-0195058239. DOI: 10.1093/acprof:oso/9780195058239.001.0001.
- [61] H. Helmholtz. “Ueber einige Gesetze der Vertheilung elektrischer Ströme in körperlichen Leitern mit Anwendung auf die thierisch-elektrischen Versuche”. In: *Annalen der Physik* 165.6 (1853), pp. 211–233. DOI: <https://doi.org/10.1002/andp.18531650603>. eprint: <https://onlinelibrary.wiley.com/doi/pdf/10.1002/andp.18531650603>. URL: <https://onlinelibrary.wiley.com/doi/abs/10.1002/andp.18531650603>.
- [62] Stanley Rush and Daniel A. Driscoll. “EEG Electrode Sensitivity-An Application of Reciprocity”. In: *IEEE Transactions on Biomedical Engineering* BME-16.1 (1969), pp. 15–22. DOI: 10.1109/TBME.1969.4502598.
- [63] Rainer Kress. *Linear Integral Equations*. 3rd ed. Applied Mathematical Sciences 82. Springer, New York, NY, 2014. DOI: <https://doi.org/10.1007/978-1-4614-9593-2>.
- [64] D. Wilton et al. “Potential integrals for uniform and linear source distributions on polygonal and polyhedral domains”. In: *IEEE Transactions on Antennas and Propagation* 32.3 (1984), pp. 276–281. DOI: 10.1109/TAP.1984.1143304.
- [65] A. Van Oosterom and J. Strackee. “The Solid Angle of a Plane Triangle”. In: *IEEE Transactions on Biomedical Engineering* BME-30.2 (1983), pp. 125–126. DOI: 10.1109/TBME.1983.325207.
- [66] MATLAB. *9.10.0.1602886 (R2021a)*. Natick, Massachusetts: The MathWorks Inc., 2021.
- [67] Sergey N. Makarov. *GitHub Repository November 2019 TMS Modeling Package v1.1 Fall 2019*. 2019. URL: <https://tmscorelab.github.io/TMS-Modeling-Website/> (visited on 2021-12-03).

- [68] Sergey N. Makarov. *Electrical stimulation with BEM-FMM—validation examples. 05.29.2 Dropbox folder*. 2021. URL: <https://www.dropbox.com/sh/gf2jpx5gi0oso8m/AADed5hdZXZExszPb60d2s1va?dl=0> (visited on 2021-12-03).
- [69] Leslie Greengard and Vladimir Jr. Rokhlin. “A fast algorithm for particle simulations”. In: *Journal of Computational Physics* 73.2 (1987), pp. 325–348. ISSN: 0021-9991. DOI: [https://doi.org/10.1016/0021-9991\(87\)90140-9](https://doi.org/10.1016/0021-9991(87)90140-9). URL: <https://www.sciencedirect.com/science/article/pii/0021999187901409>.
- [70] Barry A. Cipra. “The Best of the 20th Century: Editors Name Top 10 Algorithms”. In: *SIAM News* 33.4 (2000-05). URL: <https://archive.siam.org/news/news.php?id=637>.
- [71] Leslie Greengard and Vladimir Rokhlin. “A new version of the Fast Multipole Method for the Laplace equation in three dimensions”. In: *Acta Numerica* 6 (1997), pp. 229–269. DOI: 10.1017/S0962492900002725.
- [72] R. Beatson and Leslie Greengard. “A short course on fast multipole methods”. English (US). In: *Wavelets, multilevel methods, and elliptic PDEs*. Ed. by M. Ainsworth and al. Numerical Mathematics and Scientific Computation. Oxford University Press, 1997, pp. 1–37.
- [73] Leslie F. Greengard. *The Rapid Evaluation of Potential Fields in Particle Systems*. The MIT Press, 1988-04. ISBN: 9780262256254. DOI: 10.7551/mitpress/5750.001.0001. URL: <https://doi.org/10.7551/mitpress/5750.001.0001>.
- [74] J. Carrier, L. Greengard, and V. Rokhlin. “A Fast Adaptive Multipole Algorithm for Particle Simulations”. In: *SIAM J. Sci. Stat. Comput.* 9.4 (1988-07), pp. 669–686. ISSN: 0196-5204. DOI: 10.1137/0909044. URL: <https://doi.org/10.1137/0909044>.
- [75] Philip R. Wallace. *Mathematical Analysis of Physical Problems*. Dover Books on Physics. Dover Publications Inc., 1985. ISBN: 978-0-486-64676-3.
- [76] Zydrunas Gimbutas et al. *FMM3D*. Version py_v1.0.0. 2021-11-17. URL: <https://github.com/flatroninstitute/FMM3D>.
- [77] Johannes Vorwerk et al. “Comparison of Boundary Element and Finite Element Approaches to the EEG Forward Problem”. In: *Biomedical Engineering / Biomedizinische Technik* 57 (2012-01). DOI: 10.1515/bmt-2012-4152.
- [78] Carsten H. Wolters. “Direkte Methoden zur Berechnung dipolinduzierter elektrischer und magnetischer Felder und inverse Strategien zur Quelllokalisierung im Gehirn”. Diploma Thesis. RWTH Aachen University, 1997.
- [79] Luis J. Gomez et al. “Conditions for numerically accurate TMS electric field simulation”. In: *Brain Stimulation* 13.1 (2020), pp. 157–166. ISSN: 1935-861X. DOI: <https://doi.org/10.1016/j.brs.2019.09.015>. URL: <https://www.sciencedirect.com/science/article/pii/S1935861X1930378X>.
- [80] Zhengji Zhang. “A fast method to compute surface potentials generated by dipoles within multilayer anisotropic spheres.” In: *Physics in medicine and biology* 40 3 (1995), pp. 335–49.
- [81] Christophe Geuzaine and Jean-François Remacle. “Gmsh: A 3-D finite element mesh generator with built-in pre- and post-processing facilities”. In: *International Journal for Numerical Methods in Engineering* 79.11 (2009), pp. 1309–1331. DOI: <https://doi.org/10.1002/nme.2579>. eprint: <https://onlinelibrary.wiley.com/doi/pdf/10.1002/nme.2579>. URL: <https://onlinelibrary.wiley.com/doi/abs/10.1002/nme.2579>.

- [82] Per-Olof Persson and Gilbert Strang. “A Simple Mesh Generator in MATLAB”. In: *SIAM Review* 46.2 (2004), pp. 329–345. DOI: 10.1137/S0036144503429121. eprint: <https://doi.org/10.1137/S0036144503429121>. URL: <https://doi.org/10.1137/S0036144503429121>.
- [83] F. Sharbrough et al. “American Electroencephalographic Society guidelines for standard electrode position nomenclature”. In: *Clinical Neurophysiology* 8 (1991-01), pp. 200–202.
- [84] Jayant Acharya et al. “American Clinical Neurophysiology Society Guideline 2: Guidelines for Standard Electrode Position Nomenclature”. In: *The Neurodiagnostic Journal* 56 (2016-10), pp. 245–252. DOI: 10.1080/21646821.2016.1245558.
- [85] Paul Bourke. *Circles and spheres*. 2021-11-17. URL: <http://paulbourke.net/geometry/circlesphere/>.
- [86] Mervin E. Muller. “A Note on a Method for Generating Points Uniformly on n -Dimensional Spheres”. In: *Commun. ACM* 2.4 (1959-04), pp. 19–20. ISSN: 0001-0782. DOI: 10.1145/377939.377946. URL: <https://doi.org/10.1145/377939.377946>.
- [87] Sophie Schrader. *DUNEuro Source model parameters*. 2021. URL: <https://gitlab.dune-project.org/duneuro/duneuro/-/wikis/source-model-parameters> (visited on 2021-12-03).
- [88] D.C. Van Essen et al. “The Human Connectome Project: A data acquisition perspective”. In: *NeuroImage* 62.4 (2012). Connectivity, pp. 2222–2231. ISSN: 1053-8119. DOI: <https://doi.org/10.1016/j.neuroimage.2012.02.018>. URL: <https://www.sciencedirect.com/science/article/pii/S1053811912001954>.
- [89] Guilherme B. Saturnino et al. “SimNIBS 2.1: A Comprehensive Pipeline for Individualized Electric Field Modelling for Transcranial Brain Stimulation”. In: *Brain and Human Body Modeling: Computational Human Modeling at EMBC 2018*. Ed. by Sergey N. Makarov, Marc Horner, and Gregory Noetscher. Springer International Publishing, 2019, pp. 3–25. ISBN: 978-3-030-21293-3. DOI: 10.1007/978-3-030-21293-3_1. URL: https://doi.org/10.1007/978-3-030-21293-3_1.

Declaration of Academic Integrity

I hereby confirm that this thesis on “Comparison of Boundary Element Fast Multipole and Finite Element Methods for the solution of the EEG forward problem” is solely my own work and that I have used no sources or aids other than the ones stated. All passages in my thesis for which other sources, including electronic media, have been used, be it direct quotes or content references, have been acknowledged as such and the sources cited.

(date and signature of student)

I agree to have my thesis checked in order to rule out potential similarities with other works and to have my thesis stored in a database for this purpose.

(date and signature of student)